Supporting Information

Systematic Computational and Experimental Investigation of Lithium-ion Transport Mechanisms in Polyester-based Polymer Electrolytes

Michael A. Webb,[†] Yukyung Jung,[‡] Danielle M. Pesko,[¶] Brett M. Savoie,[†] Umi Yamamoto,[†] Geoffrey W. Coates,[‡] Nitash P. Balsara,[¶,§,‖] Zhen-Gang Wang,[†] and Thomas F. Miller III[*,†]

Department of Chemistry and Chemical Engineering, California Institute of Technology, Pasadena, California 91125, USA,

Department of Chemistry and Chemical Biology, Baker Laboratory, Cornell University, Ithaca, New York 14853, USA,

Department of Chemical and Biomolecular Engineering, University of California, Berkeley, Berkeley, California 94720, USA,

Materials Science Division, Lawrence Berkeley National Laboratory, Berkeley, California 94720, USA, and

Environmental Energy Technology Division, Lawrence Berkeley National Laboratory, Berkeley, California 94720, USA

E-mail: tfm@caltech.edu

[*]To whom correspondence should be addressed
[†]California Institute of Technology
[‡]Cornell University
[¶]University of California, Berkeley
[§]LBNL- Materials Science Division
[‖]LBNL - Environmental Energy Technology Division

Contents

1 Synthesis Details **SI-4**

1.1 General Considerations: Synthesis SI-4

1.2 Materials SI-4

1.3 Synthesis of 2-((2-(2-Methoxyethoxy)ethoxy)methyl)oxirane SI-5

1.4 Synthesis of Catalysts SI-6

1.4.1 Salicylaldehyde Synthesis SI-6

1.4.2 N, N'-Bis(3-methyl-5-fluoro-salicylidene)-1,2-cyclohexadiimine Synthesis SI-9

1.4.3 (F-salcy)Cobalt(III)NO_3 Complex Synthesis SI-9

1.4.4 (*tert*-Butyl-salcy)Cobalt(III)NO_3 Complex Synthesis SI-10

1.5 Copolymerization Procedures SI-14

1.5.1 Synthesis of Polymer 1a SI-14

1.5.2 Synthesis of Polymer 1b SI-14

1.5.3 Synthesis of Polymer 2a SI-14

1.5.4 Synthesis of Polymer 2b SI-15

1.5.5 Synthesis of Polymer 3a SI-15

1.5.6 Synthesis of Polymer 3b SI-15

1.6 NMR Spectra for Polyesters SI-16

1.6.1 Polymer 1a SI-16

1.6.2 Polymer 1b SI-18

1.6.3 Polymer 2a SI-20

1.6.4 Polymer 2b SI-22

1.6.5 Polymer 3a SI-24

1.6.6 Polymer 3b SI-26

2 Simulation Protocol Details **SI-28**

3 Electrochemical Characterization Details **SI-30**

4 Repeat Units and Terminal Groups for Polyesters in MD Simulations SI-31

5 Force Field Parameters for Molecular Dynamics Simulations SI-33

5.1 Non-bonded Interaction Parameters SI-34

5.2 Bonding Potential Parameters SI-35

5.3 Bending Potential Parameters SI-36

5.4 Torsional Potential Parameters SI-37

6 Apparent Diffusivities in Simulation SI-39

7 Experimental Dilute-ion Conductivities SI-41

8 Effect of Terminal Group Interactions in Polymer 1a SI-44

9 Correlation between T_g and Conductivity in MD Simulations SI-46

10 Radial Distribution Functions for all Polymers SI-47

11 Side chain Localization of Lithium Cation in Polymer 3a SI-48

12 Backbone Localization of Lithium Cation in Type-1 and -2 Polymers SI-49

13 Comparison of Solvation-Site Networks SI-51

1 Synthesis Details

1.1 General Considerations: Synthesis

All air and water sensitive compounds were handled under dry nitrogen using a Braun Labmaster Glovebox or standard Schlenk line techniques. ^{1}H and ^{13}C NMR spectra were recorded on a Varian INOVA 400 (^{1}H, 400 MHz) or Varian INOVA 500 (^{1}H, 500 MHz) spectrometer. ^{1}H NMR spectra were referenced with residual non-deuterated solvent shifts ($CHCl_3$= 7.26 ppm) and ^{13}C NMR spectra were referenced by solvent shifts ($CDCl_3$= 77.16 ppm). Gel permeation chromatography (GPC) was performed using an Agilent PL-GPC 50 integrated system (2 x PLgel Mini-MIX C columns, 5 micron, 4.6 mmID) equipped with a refractive index detector. The GPC columns were eluted with tetrahydrofuran at a rate of 0.3 mL/min at 30 ℃, and samples were calibrated relative to polystyrene standards. Differential scanning calorimetry (DSC) was performed on a Mettler-Toledo Polymer DSC instrument equipped with a Julabo chiller and autosampler. DSC polymer samples were prepared in crimped aluminum pans. All of the polyesters were analyzed using the following DSC protocol: heating under nitrogen from -70 ℃ to 200 ℃ at 10 ℃/min, cooling from 200 ℃ to -70 ℃ at 10 ℃/min, and then heating from -70 ℃ to 200 ℃ at 10 ℃/min. The data were processed using StarE software, and all reported glass transition temperatures were obtained from the second heating cycle.

1.2 Materials

Calcium hydride (90%, Strem) was used as received to dry the epoxides. (*S*)-Propylene oxide (Sigma-Aldrich) and allyl glycidyl ether (Sigma-Aldrich) were dried over calcium hydride for 3 days, vacuum-transferred to a dry Schlenk adapted flask, and degassed via 3 freeze-pump-thaw cycles. The synthesis of 2-((2-(2-methoxyethoxy)ethoxy)methyl)oxirane is described below. The purified 2-((2-(2-methoxyethoxy)ethoxy)methyl)oxirane was dried over calcium hydride overnight, distilled into a dry Schlenk adapted flask, and degassed via

3 freeze-pump-thaw cycles. Glutaric anhydride (Acros, 97%) was purified by suspending in dichloromethane and washing with saturated aqueous sodium bicarbonate. The organic layer was dried over Na_2SO_4, filtered, and concentrated. The residue was washed with ether, then dried under reduced pressure and sublimed. Diglycolic anhydride (Alfa Aesar, 97%) was purified by sublimation. All epoxides and anhydrides were stored in the glovebox immediately following purification. Metal precursor $Co(NO_3)_2{\cdot}6H_2O$ (>99% purity) was purchased from Strem and stored in a desiccator. Toluene and dichloromethane were purchased from Fisher Scientific and purified using a Phoenix solvent drying system. Bis(triphenylphosphine)iminium chloride (PPNCl) was purchased from Sigma-Aldrich and recrystallized by layering dichloromethane and diethyl ether. NMR solvents were purchased from Cambridge Isotopes and stored over 3 Å molecular sieves. All other reagents were purchased from commercial sources and used as received.

1.3 Synthesis of 2-((2-(2-Methoxyethoxy)ethoxy)methyl)oxirane

Sodium hydride (60% in mineral oil, 5.65 g, 141 mmol) was added to a 250 mL round bottom flask under nitrogen, then 160 mL of dried, degassed THF was added via cannula. The flask was cooled to 0 ℃ , and diethylene glycol methyl ether (13.3 mL, 113 mmol) was added dropwise. The reaction was stirred for 30 minutes at 0 ℃ , and then epichlorohydrin (22.1 mL, 282 mmol) was added dropwise. The reaction was warmed to room temperature, refluxed for 2 hours under nitrogen, and then cooled to room temperature and stirred overnight. The reaction was quenched with 20 mL ethanol, filtered through a pad of Celite, and then concentrated to give a cloudy yellow oil. The crude product was distilled under reduced pressure to yield 12.6 g (63% yield) of the product as a clear liquid. The ^{1}H NMR matched those previously reported in the literature.[1] ^{1}H NMR spectrum in ppm ($CDCl_3$, 400 MHz): δ 3.68 (dd, 1 H, J =3.0, 11.6); 3.51-3.65 (m, 6H); 3.42-3.47 (m, 2H); 3.33 (q, 1 H, J =5.9, 11.7 Hz); 3.27 (s, 3H); 3.05 (m, 1 H), 2.68 (t, 1 H, J =4.7 Hz), 2.50 (dd, 1 H, J =2.7, 5.0 Hz).

1.4 Synthesis of Catalysts

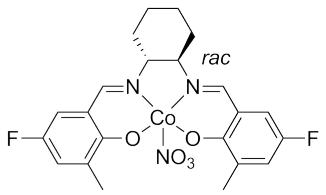

Catalyst 1

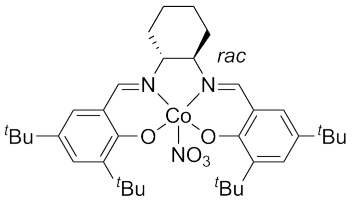

Catalyst 2

The synthesis of catalyst 1 is described below. The ligand for catalyst 2 (N, N'-bis (3, 5-*tert*-butyl-salicylidene)-1,2-cyclohexadiimine) was synthesized following literature procedures,[2] and the synthesis of the complex is described below.

1.4.1 Salicylaldehyde Synthesis

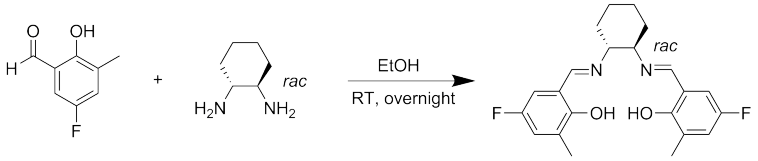

The salicylaldehyde was synthesized from 5-methyl-3-fluorophenol using a modified Duff reaction as reported by Jacobsen et al.[3] The product was purified by column chromatography (10% ether in hexanes to 15% ether in hexanes) to yield the product as a yellow crystalline solid in 18% isolated yield. The ^{1}H NMR spectrum of the ligand precursor, 5-methyl-3-fluorosalicylaldehyde, matches that previously reported in the literature.[4] ^{1}H NMR spectrum in ppm ($CDCl_3$, 500 MHz): δ 11.05 (s, 1 H); 9.81 (s, 1 H); 7.14 (dd, J =2.1, 8.7, 1 H); 7.06 (dd, J =3.1, 7.6, 1 H), 2.27 (s, 3H). ^{13}C NMR spectrum in ppm ($CDCl_3$, 125 MHz): δ 195.79; 156.45; 155. 33 (J_{CF} =239.4 Hz); 129.47; 125.46; 119.40; 115.21; 15.32. HR/MS: calculated 154.04301 g/mol; found 154.06623 g/mol.

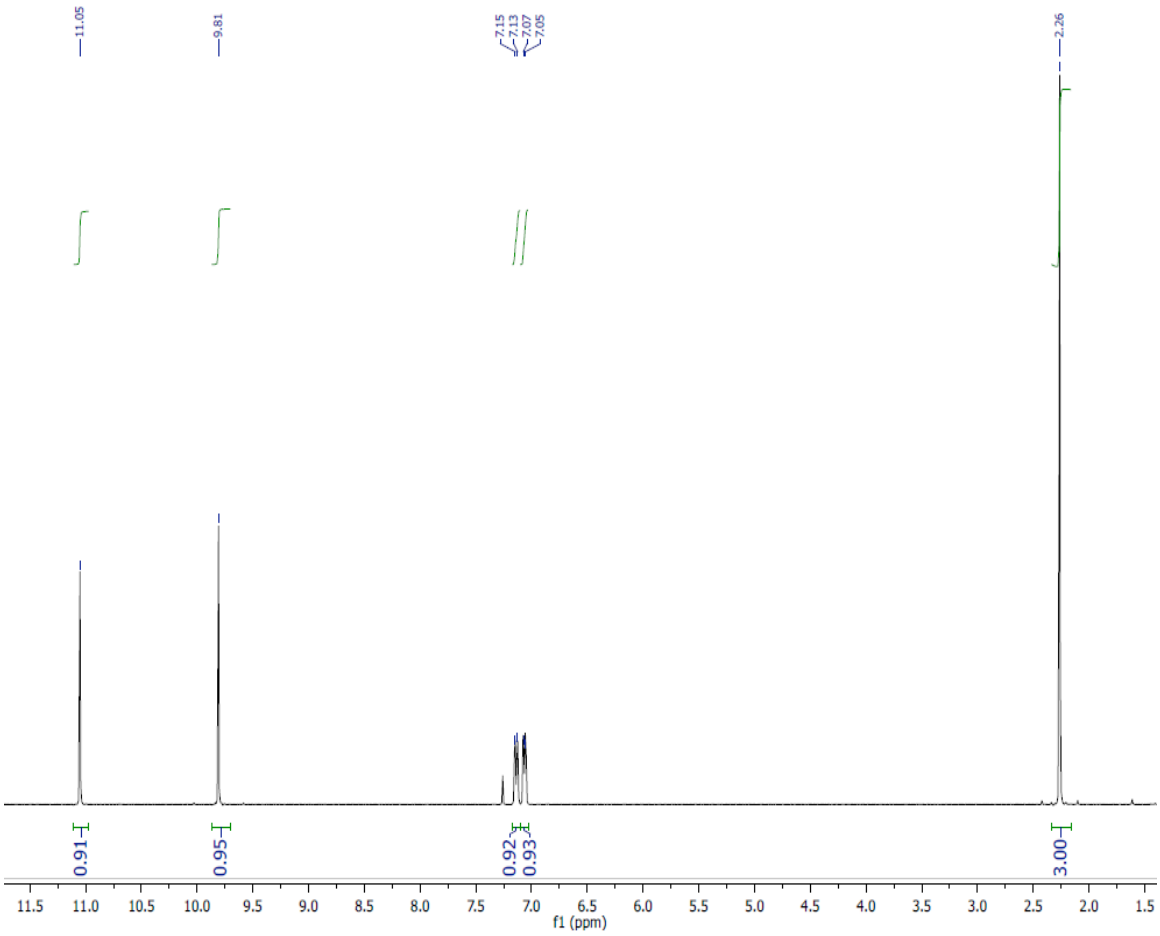

Figure S1: ^{1}H NMR spectrum of 5-methyl-3-fluorosalicylaldehyde in $CDCl_3$.

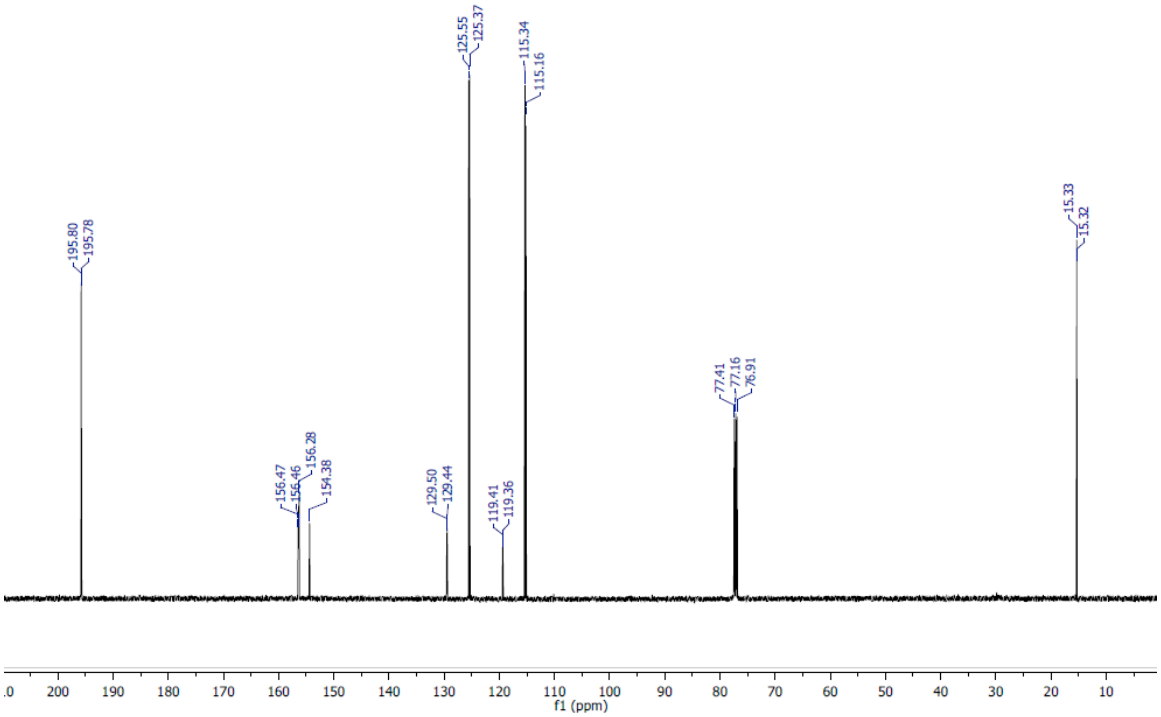

Figure S2: ^{13}C NMR spectrum of 5-methyl-3-fluorosalicylaldehyde in $CDCl_3$.

1.4.2 N, N'-Bis(3-methyl-5-fluoro-salicylidene)-1,2-cyclohexadiimine Synthesis

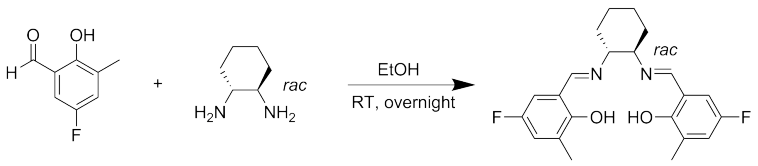

The salicylaldehyde (431.4 mg, 2.8 mmol) was dissolved in 7 mL of absolute EtOH at room temperature. The racemic *trans*-1,2-diaminocyclohexane (168 μL, 1.4 mmol) was added, and a yellow precipitate was observed after about 10 minutes of stirring. The reaction was stirred at room temperature overnight. The mixture was diluted with 2 mL of water, and the yellow solid was isolated by vacuum filtration. The solid was dried under vacuum to give the ligand in 82% yield (445.9 mg). ^{1}H NMR spectrum in ppm ($CDCl_3$, 500 MHz): δ 13.27 (s, 1 H); 8.18 (s, 2H); 6.87 (dd, J =2.9, 9.0, 2H); 6.70 (dd, J =3.0, 8.3, 2H); 3.31 (m, 2H); 2.23 (s, 6H); 1.40-2.00 (m, 8H). ^{13}C NMR spectrum in ppm ($CDCl_3$, 125 MHz): δ 164.10; 155. 49; 154.93; 127.76; 120.37; 117.46; 113.87; 72.77; 33.19; 24.25; 15.71. HR/MS: calculated 387.18786 g/mol (M+H); found 387.18735 g/mol.

1.4.3 (F-salcy)Cobalt(III)NO_3 Complex Synthesis

The (F-salcy)cobalt(III)NO_3 complex was synthesized according to literature procedure.[5] The ligand, N, N'-bis(3-methyl-5-fluoro-salicylidene)-1,2-cyclohexadiimine (350 mg, 0.906 mmol), was dissolved in dichloromethane in a flame-dried Schlenk flask under nitrogen. In a separate flame-dried Schlenk flask, $Co(NO_3)_2{\cdot}6H_2O$ was dehydrated by heating to 60 ℃ under reduced pressure until the color changed from red to light pink. The dehydrated $Co(NO_3)_2{\cdot}6H_2O$ was dissolved in anhydrous, degassed ethanol and subsequently added to the ligand solution via cannula. The mixture was stirred for 15 minutes under nitrogen, then exposed to dry air by attaching a drying tube charged with Drierite to the top of the flask. The reaction was stirred under dry air overnight to oxidize the complex. The reaction mixture was evacuated to dryness, washed with pentanes, and dried under reduced

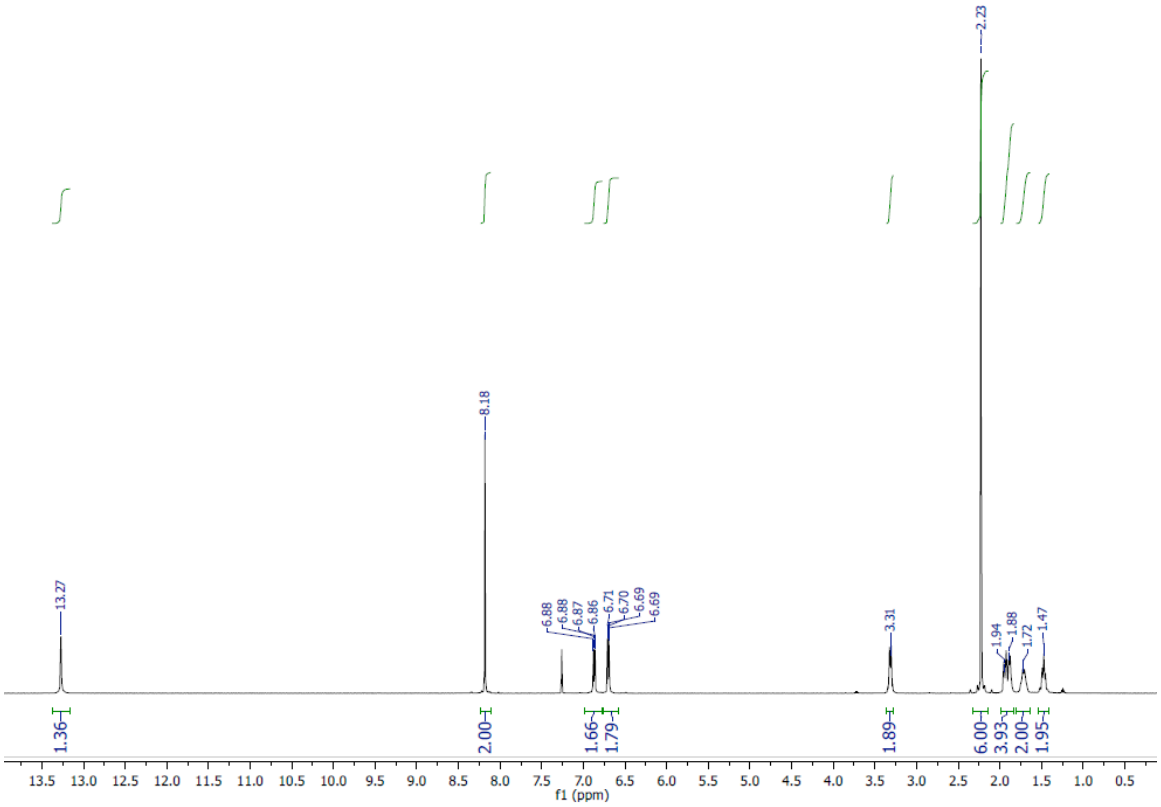

Figure S3: ^{1}H NMR spectrum of N,N'-bis(3-methyl-5-fluoro-salicylidene)-1,2-cyclohexadiimine in $CDCl_3$.

pressure. The resulting dark green powder (396.4 mg, 86% isolated yield) was stored in a glovebox under nitrogen. ^{1}H NMR spectrum (C_5D_5N, 500 MHz): δ 8.83 (2H); 7.39 (2H); 4.16 (^{1}H); 3.21 (^{1}H); 2.83 (6H); 1.5-2.3 (8H). ^{13}C NMR spectrum (C_5D_5N, 125 MHz): δ 167.27; 161.53; 154.41; 139.66; 134.06; 117.31; 116.40; 71.55; 30.85; 25.35; 18.01. HR/MS: calculated 443.09813 g/mol (for salcyCo^{+}); found 443.09727 g/mol.

1.4.4 (*tert*-Butyl-salcy)Cobalt(III)NO_3 Complex Synthesis

The (*tert*-Butyl-salcy)Cobalt(III)NO_3 complex was synthesized following the same procedure as in 4.3 using the N, N'-bis(3, 5-*tert*-butyl-salicylidene)-1,2-cyclohexadiimine ligand.

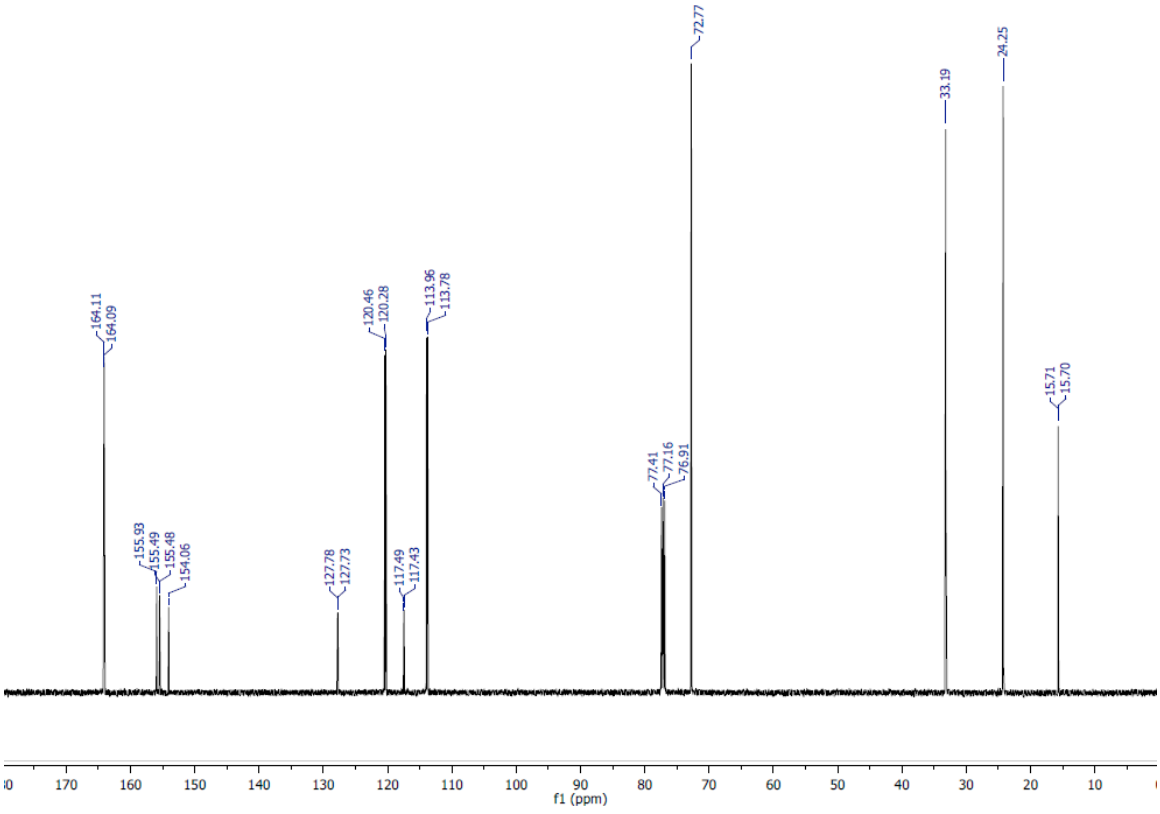

Figure S4: ^{13}C NMR spectrum of N,N'-bis(3-methyl-5-fluoro-salicylidene)-1,2-cyclohexadiimine in $CDCl_3$.

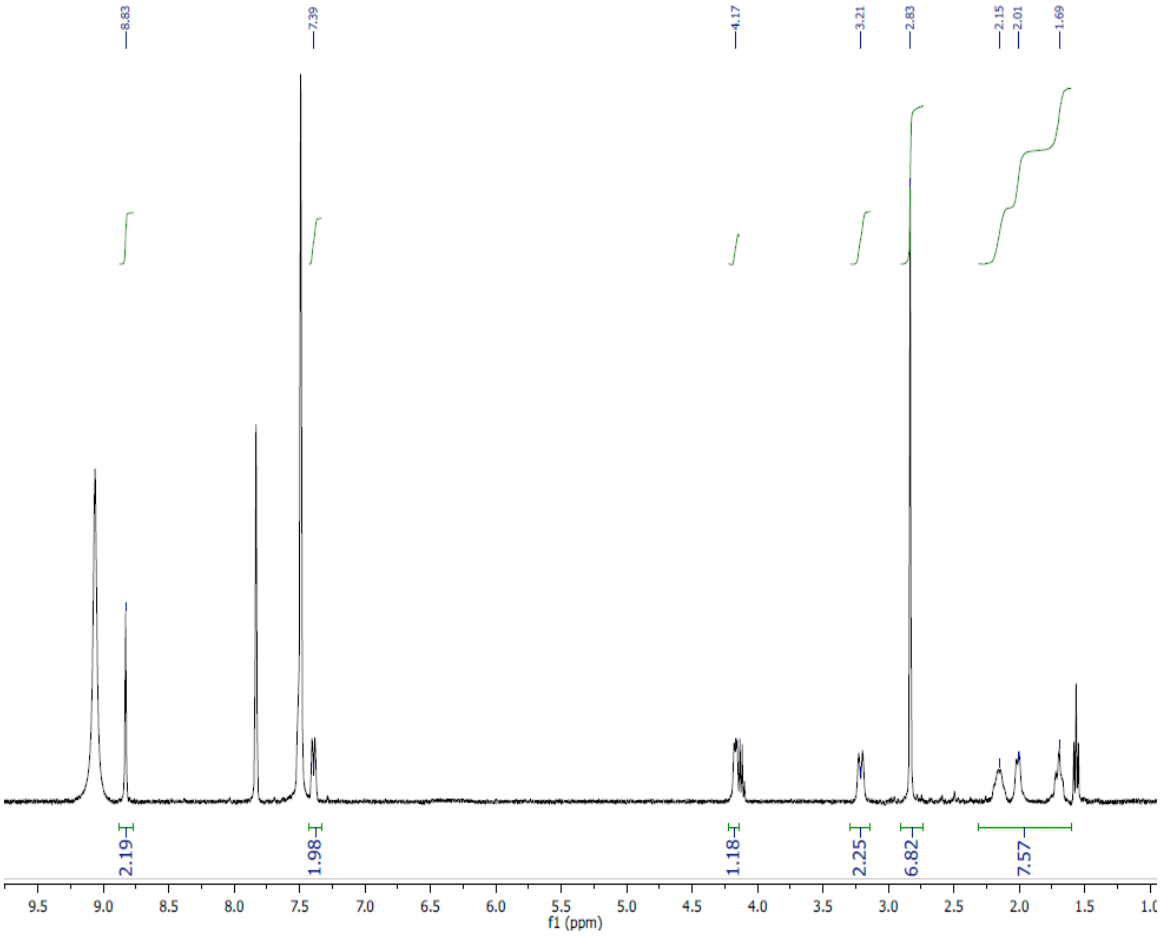

Figure S5: ^{1}H NMR spectrum of (F-salcy)cobalt(III)NO_3 complex in C_5D_5N.

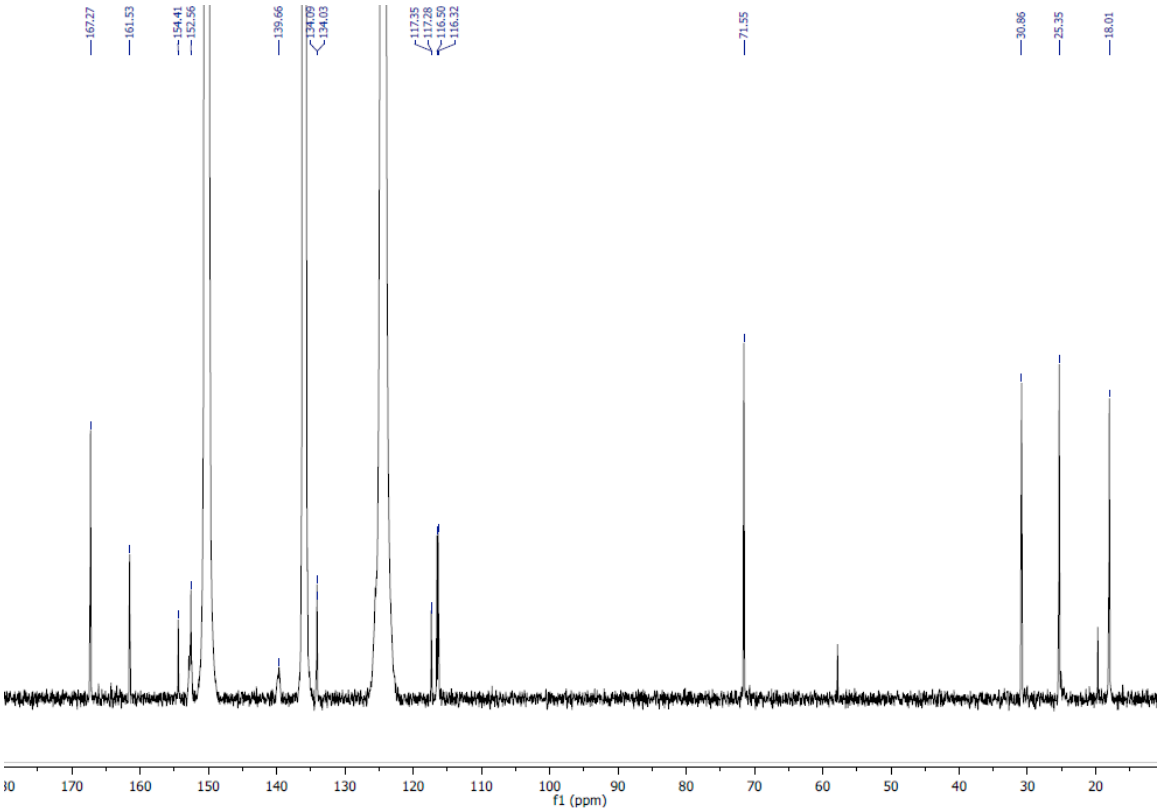

Figure S6: ^{13}C NMR spectrum of (F-salcy)cobalt(III)NO_3 complex in C_5D_5N.

1.5 Copolymerization Procedures

1.5.1 Synthesis of Polymer 1a

In the glovebox, catalyst 1(12.6 mg, 0.025 mmol), PPNCl (14.4 mg, 0.025 mmol), glutaric anhydride (850 mg, 7.5 mmol), and 0.66 mL toluene were added to a dry 4mL scintillation vial equipped with a stirbar. The epoxide (*S*)-propylene oxide (0.61 mL, 8.7 mmol) was added via syringe, and the vial was sealed with a Teflon lined cap. The reaction vial was then removed from the glovebox and stirred at 50 ℃ for 19 h. The polymerization was quenched with a solution of 5 equiv. (relative to catalyst) *p*-toluenesulfonic acid in acetone, diluted with a minimum volume of dichloromethane, and precipitated into hexanes. The precipitation process was repeated until no residual monomer was observed by ^{1}H NMR spectroscopy. The polymer was dried under reduced pressure at room temperature overnight.

1.5.2 Synthesis of Polymer 1b

Catalyst 1 (9.6 mg, 0.019 mmol), PPNCl (10.7 mg, 0.019 mmol), diglycolic anhydride (650 mg, 5.6 mmol), and 0.5 mL toluene were added to a dry 4 mL scintillation vial with a stirbar. The epoxide (*S*)-propylene oxide (0.52 mL, 7.4 mmol) was added via syringe, and the vial was sealed with a Teflon lined cap. The reaction was stirred for 20 h at 55 ℃ , and quenched with 5 equiv. of *p*-toluenesulfonic acid in acetone (relative to catalyst), and precipitated in methanol. The polymer was dried under vacuum at room temperature overnight.

1.5.3 Synthesis of Polymer 2a

Catalyst 1 (7.1 mg, 0.014 mmol), PPNCl (8.0 mg, 0.014 mmol), glutaric anhydride (480 mg, 4.2 mmol), and 0.5 mL toluene were added to a dry 4 mL scintillation vial with a stirbar. The epoxide allyl glycidyl ether (0.5 mL, 4.2 mmol) was added via syringe, and the vial was sealed with a Teflon lined cap. The reaction was stirred at 55 ℃ for 22 h and quenched with 5 equiv. of *p*-toluenesulfonic acid (relative to catalyst) in acetone. The polymer was

precipitated in MeOH and dried under vacuum at room temperature overnight.

1.5.4 Synthesis of Polymer 2b

Catalyst 1 (7.1 mg, 0.014 mmol), PPNCl (8.0 mg, 0.014 mmol), diglycolic anhydride (489 mg, 4.2 mmol), and 0.3 mL toluene were added to a dry 4 mL scintillation vial with a stirbar. The epoxide allyl glycidyl ether (0.5 mL, 4.2 mmol) was added via syringe, and the vial was sealed with a Teflon lined cap. The reaction was stirred at 25 ℃ for 25 h, and quenched with 5 equiv. of *p*-toluenesulfonic acid (relative to catalyst) in acetone. The polymer was precipitated in methanol and dried under vacuum at room temperature overnight.

1.5.5 Synthesis of Polymer 3a

Catalyst 1 (6.8 mg, 0.013 mmol), PPNCl (7.7 mg, 0.013 mmol), glutaric anhydride (450 mg, 3.9 mmol), and 0.3 mL toluene were added to a dry 4 mL scintillation vial with a stirbar. The epoxide 2-((2-(2-methoxyethoxy)ethoxy)methyl)oxirane (500 mg, 4.6 mmol) was added via syringe, and the vial was sealed with a Teflon lined cap. The reaction was stirred at 55 ℃ for 25 h, and quenched with 5 equiv. of *p*-toluenesulfonic acid (relative to catalyst) in acetone. The polymer was precipitated in hexanes and dried under vacuum at room temperature overnight.

1.5.6 Synthesis of Polymer 3b

Catalyst 2 (4.0 mg, 0.0080 mmol), PPNCl (4.6 mg, 0.0090 mmol), diglycolic anhydride (458 mg, 4.0 mmol), and 0.3 mL toluene were added to a dry 4 mL scintillation vial with a stirbar. The epoxide 2-((2-(2-methoxyethoxy)ethoxy)methyl)oxirane was added via syringe, and the vial was sealed with a Teflon lined cap. The reaction was stirred at 55 ℃ for 28 h, and quenched with 5 equiv. of *p*-toluenesulfonic acid (relative to catalyst) in acetone. The polymer was precipitated in hexanes and dried under vacuum at room temperature overnight.

1.6 NMR Spectra for Polyesters

1.6.1 Polymer 1a

^{1}H NMR spectrum ($CDCl_3$, 500 MHz): δ 5.13 (m, 1 H); 4.18 (dd, J =3.4, 11.7 Hz, 1 H); 4.03 (dd, J =6.6, 11.8 Hz, 1 H); 2.38 (dt, J =7.4, 7.4, 11.4 Hz, 4H); 1.93 (tt, J =7.3, 7.3, 7.4, 7.4 Hz, 2H); 1.24 (d, J =6.5 Hz, 3H). ^{13}C NMR spectrum ($CDCl_3$, 125 MHz): δ 172.67; 172.34; 68.34; 66.14; 33.44; 33.09; 20.12; 16.66.

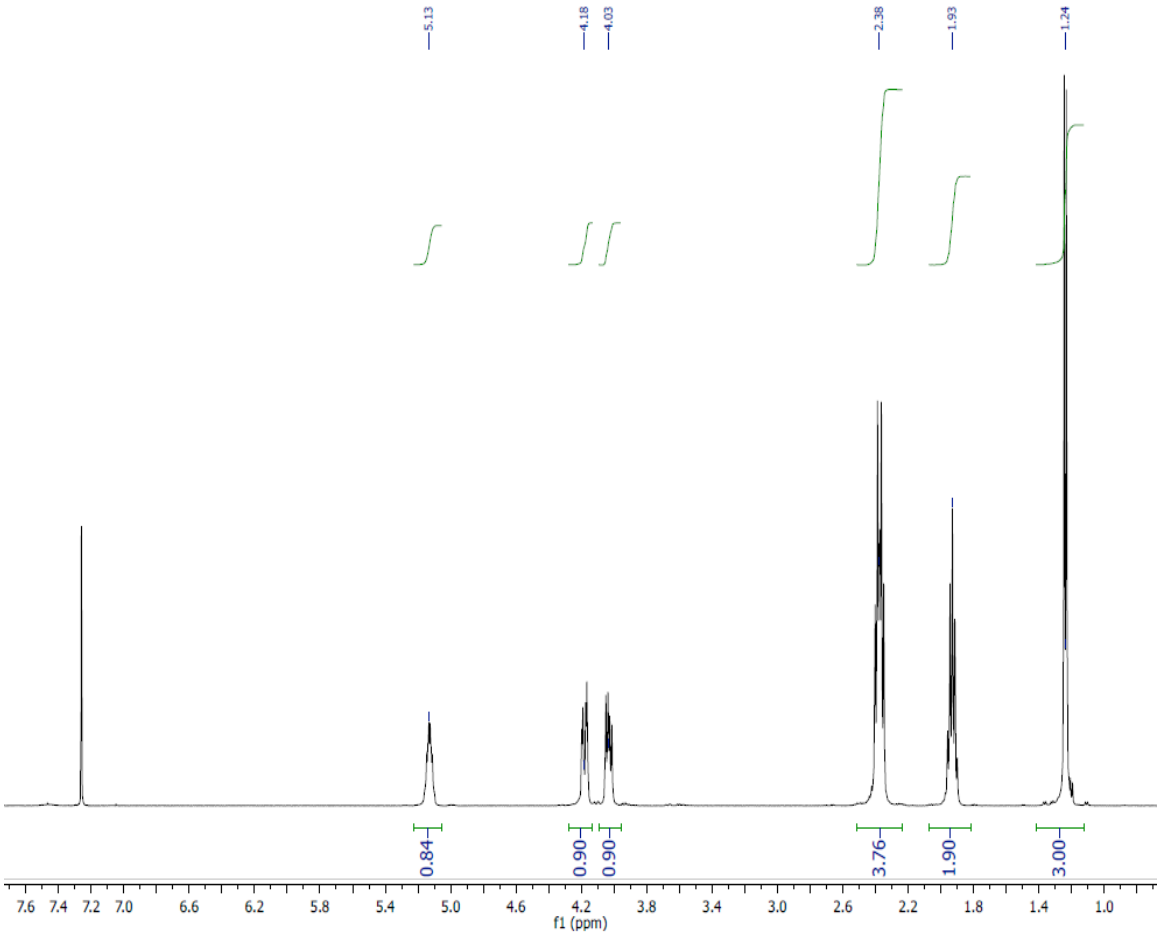

Figure S7: ^{1}H NMR spectrum of polymer 1a in $CDCl_3$.

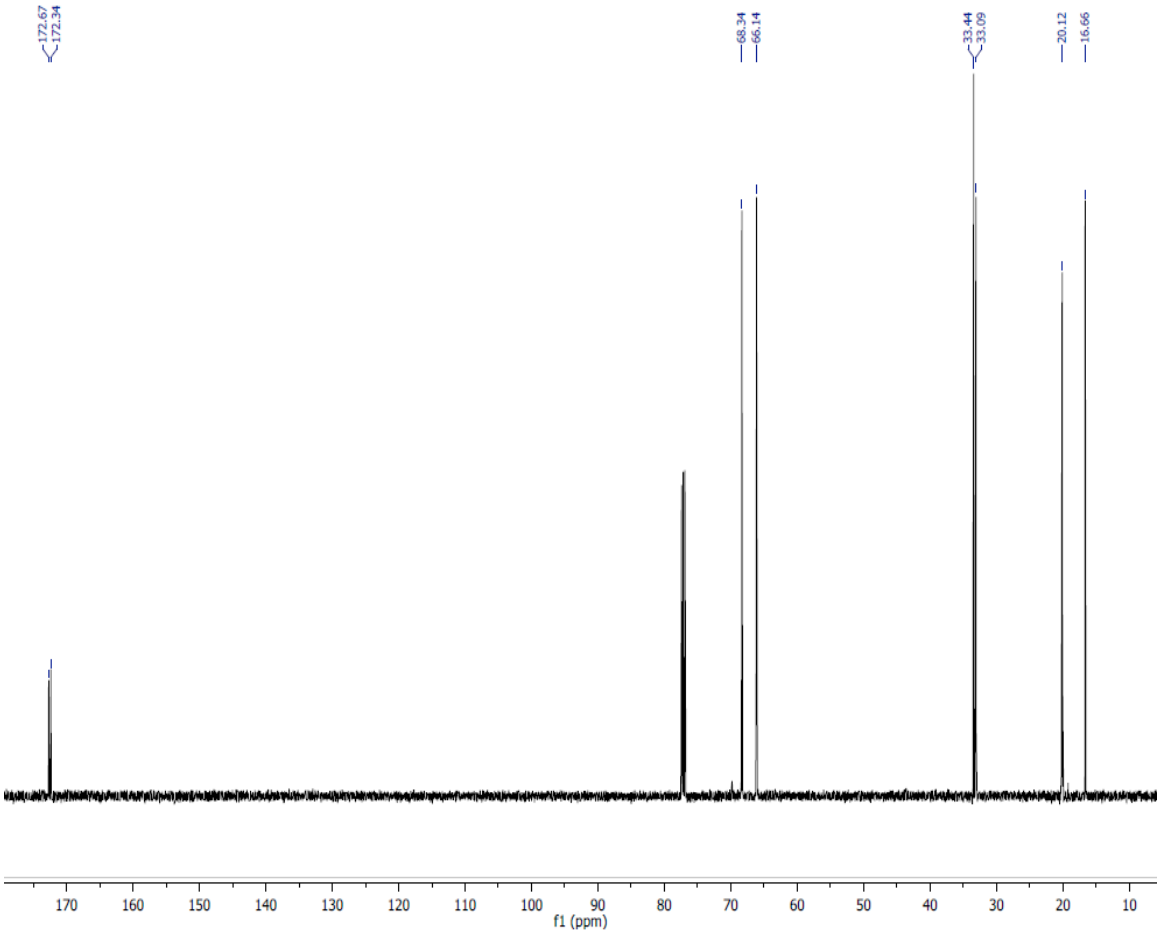

Figure S8: ^{13}C NMR spectrum of polymer 1a in $CDCl_3$.

1.6.2 Polymer 1b

^{1}H NMR spectrum ($CDCl_3$, 500 MHz): δ 5.21 (br s, 1 H); 4.20 (m, 4H); 3.98-4.43 (m, 2H); 1.26 (d, J =5.9, 3H). ^{13}C NMR spectrum ($CDCl_3$, 125 MHz): δ 169.47; 169.19; 68.97; 68.09; 67.89; 66.25; 16.41.

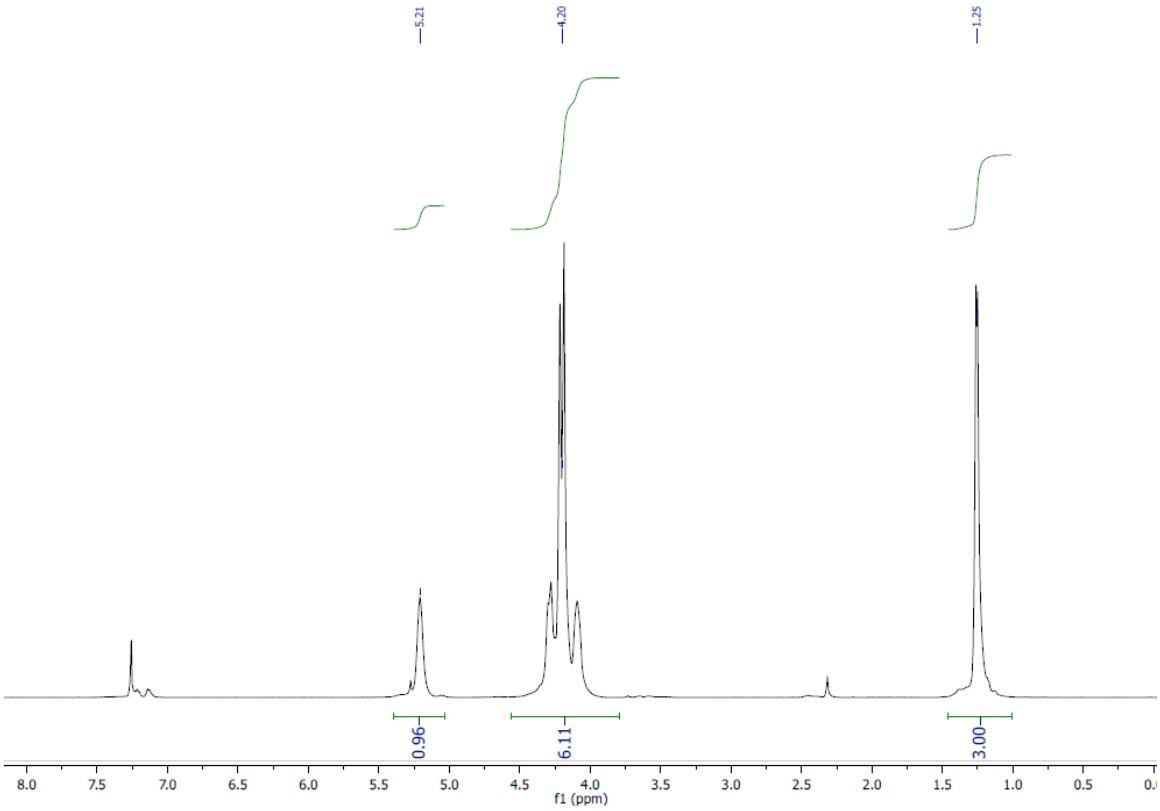

Figure S9: ^{1}H NMR spectrum of polymer 1b in $CDCl_3$.

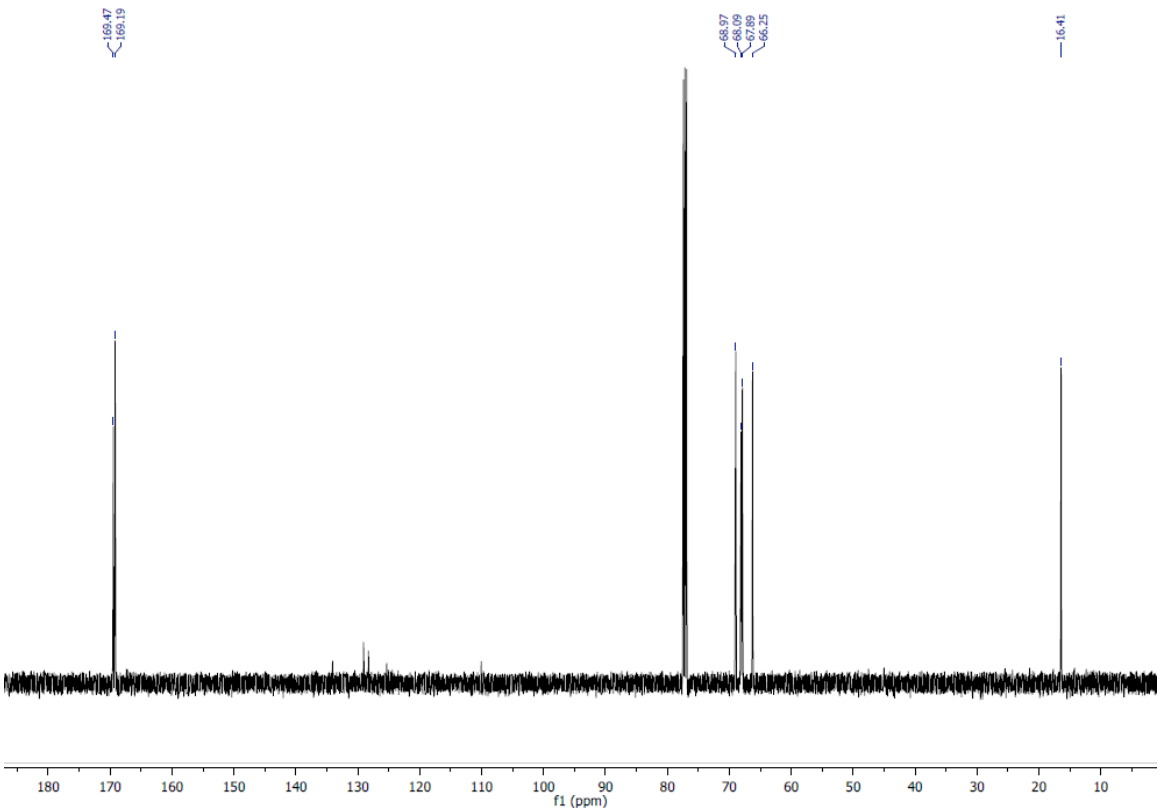

Figure S10: ^{13}C NMR spectrum of polymer 1b in $CDCl_3$.

1.6.3 Polymer 2a

^{1}H NMR spectrum ($CDCl_3$, 500 MHz): δ 5.83 (m, 1 H); 5.27-5.33 (m, 1 H); 5.18 (m, 2H); 4.33 (m, 1 H); 4.14 (m, 1 H); 3.97 (br s, 1 H); 3.53 (m, 2H); 2.37 (m, 4H); 1.92 (m, 2H). ^{13}C NMR spectrum ($CDCl_3$, 125 MHz): δ 172.54; 172.23; 134.26; 117.54; 72.35; 70.35; 68.23; 62.89; 33.25; 32.98; 20.04.

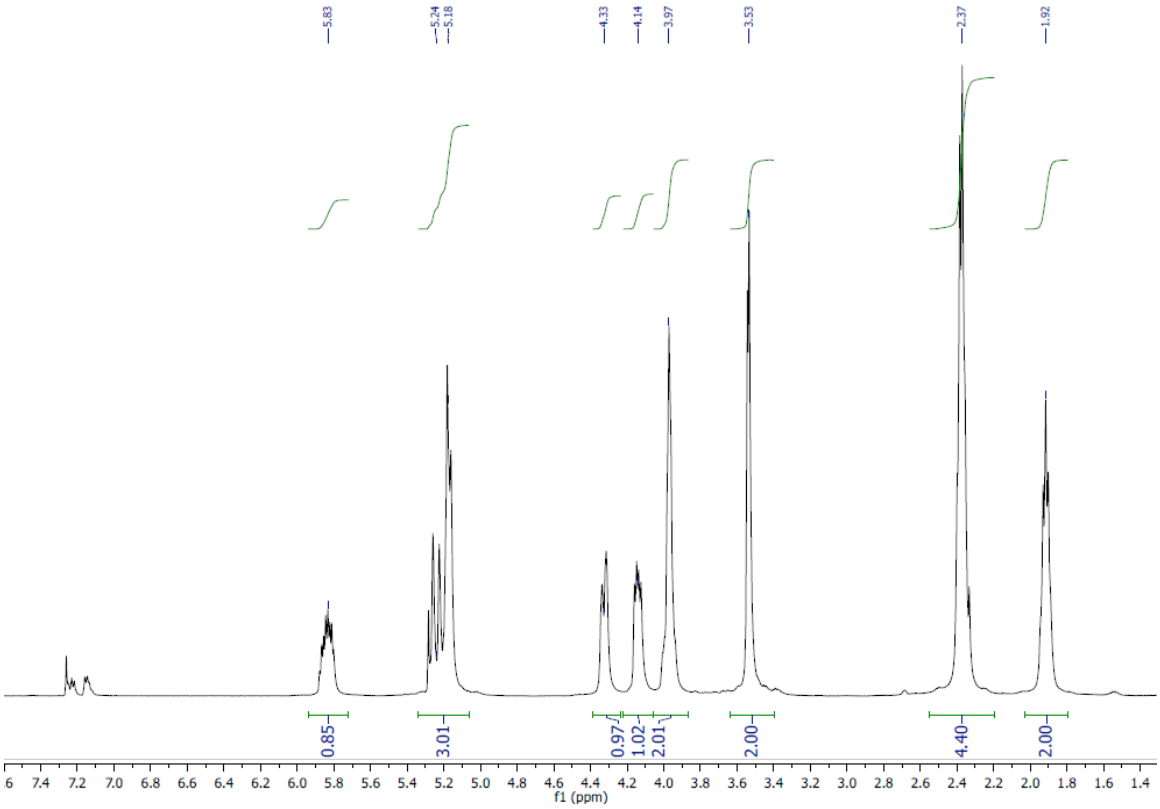

Figure S11: ^{1}H NMR spectrum of polymer 2a in $CDCl_3$.

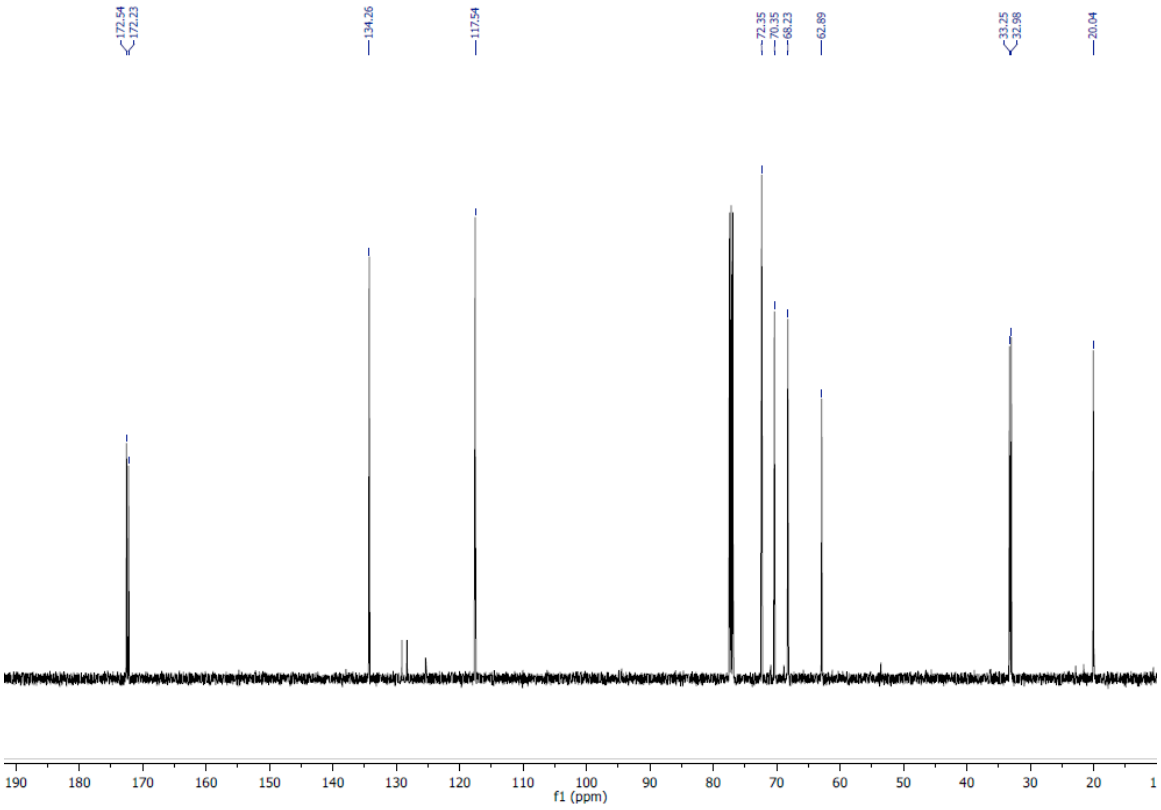

Figure S12: ^{13}C NMR spectrum of polymer 2a in $CDCl_3$.

1.6.4 Polymer 2b

^{1}H NMR spectrum ($CDCl_3$, 500 MHz): δ 5.83 (m, 1 H); 5.27-5.33 (m, 1 H); 5.18 (m, 2H); 4.33 (m, 1 H); 4.14 (m, 1 H); 3.97 (br s, 1 H); 3.53 (m, 2H); 2.37 (m, 4H); 1.92 (m, 2H). ^{13}C NMR spectrum ($CDCl_3$, 125 MHz): δ 172.54; 172.23; 134.26; 117.54; 72.35; 70.35; 68.23; 62.89; 33.25; 32.98; 20.04.

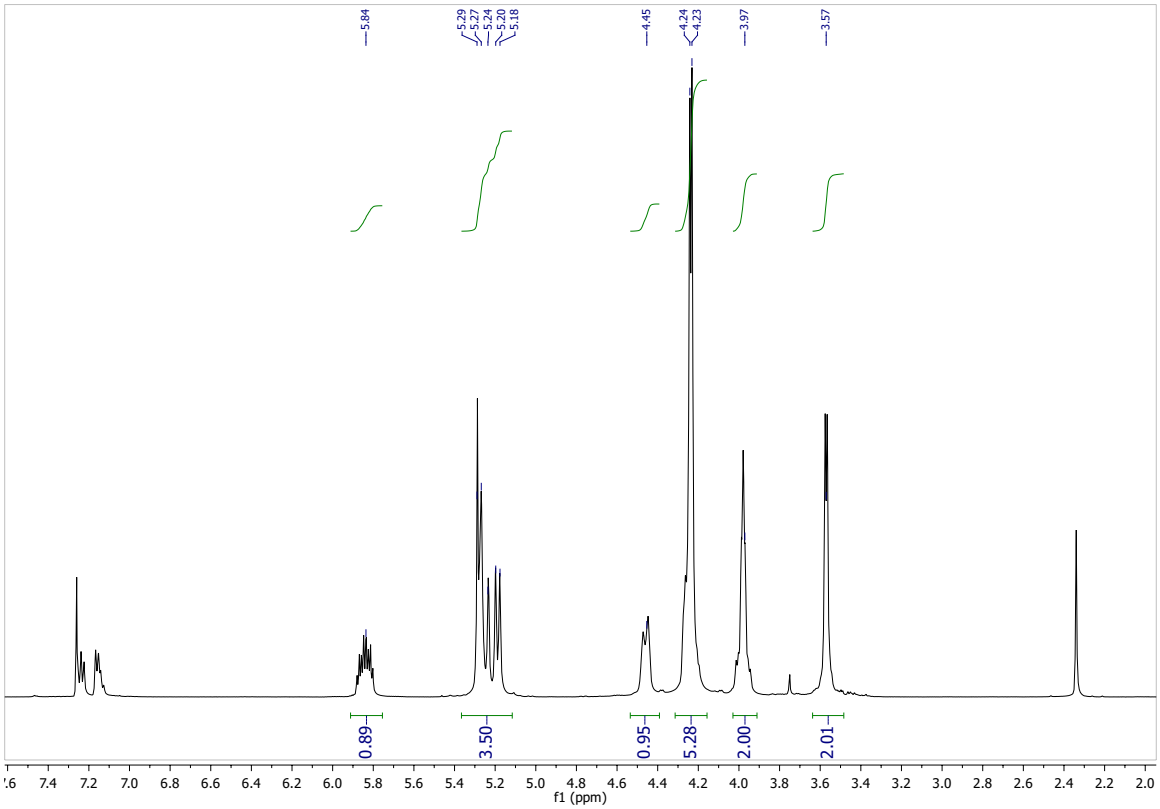

Figure S13: ^{1}H NMR spectrum of polymer 2b in $CDCl_3$.

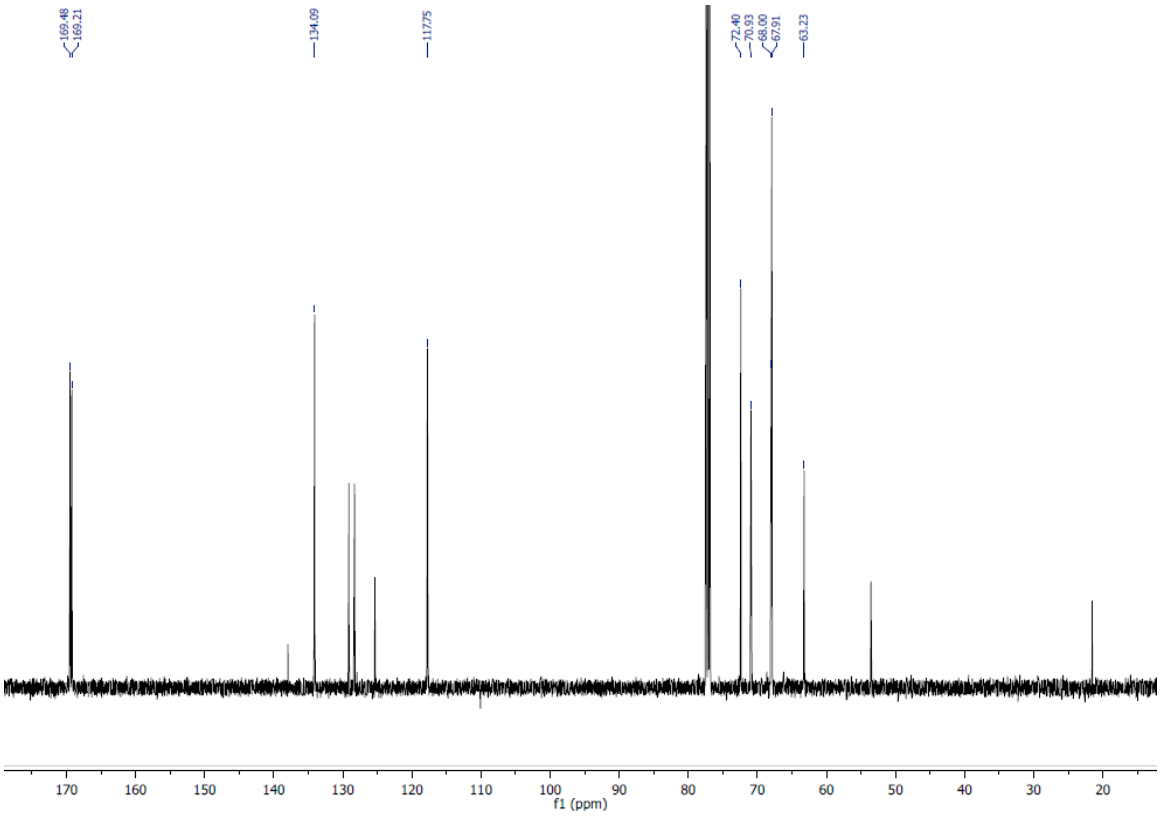

Figure S14: ^{13}C NMR spectrum of polymer 2b in $CDCl_3$.

1.6.5 Polymer 3a

^{1}H NMR spectrum ($CDCl_3$, 500 MHz): δ 5.18 (br s, 1 H); 4.34 (m, 1 H); 4.12 (m, 1 H); 3.25-3.80 (m, 10 H); 3.36 (s, 3H); 2.37 (m, 4H); 1.91 (m, 2H). ^{13}C NMR spectrum ($CDCl_3$, 125 MHz): δ 172.63; 172.34; 72.02; 71.03; 70.67; 70.64; 70.36; 69.54; 69.62; 63.07; 62.95; 59.14; 33.27; 33.02; 20.04.

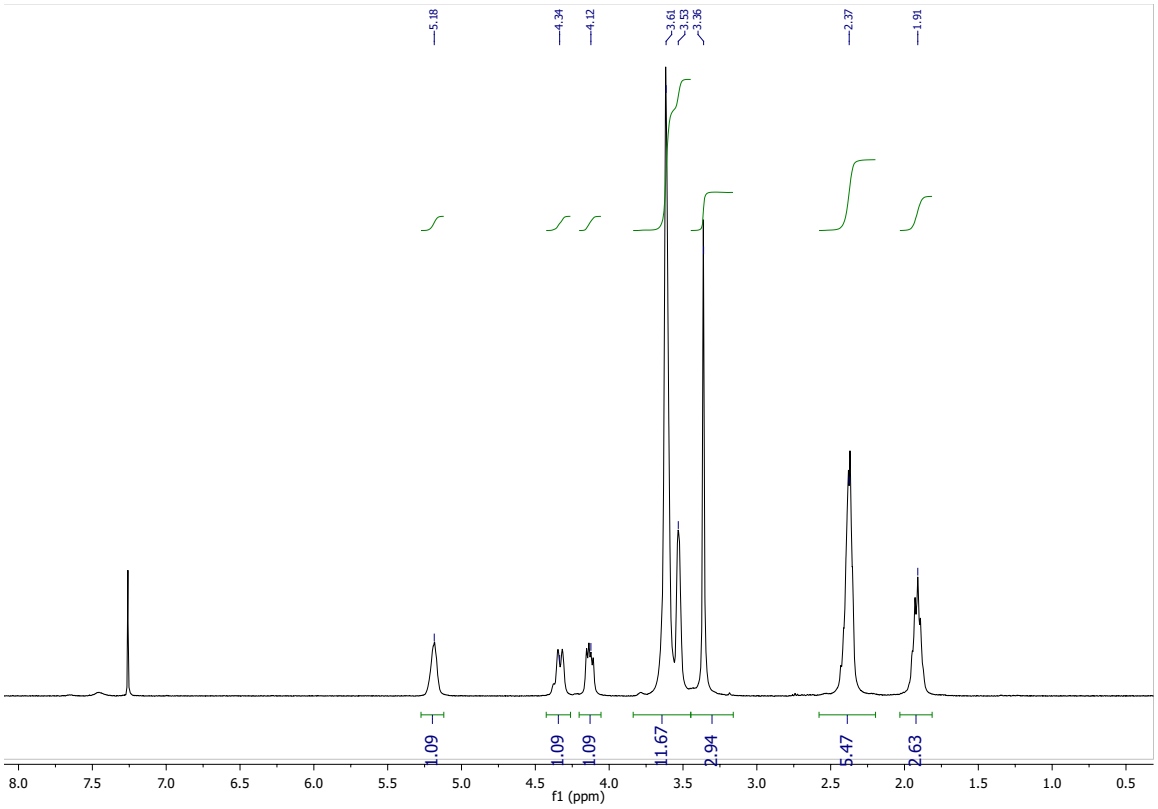

Figure S15: ^{1}H NMR spectrum of polymer 3a in $CDCl_3$.

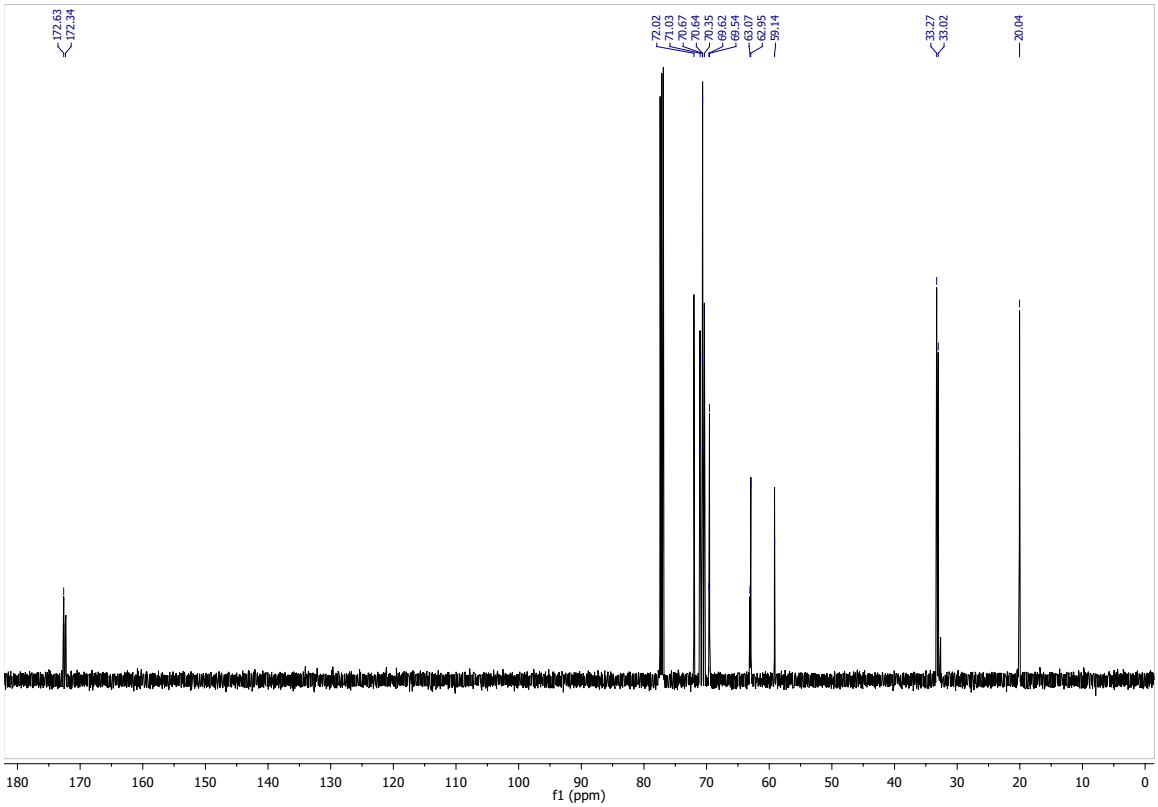

Figure S16: ^{13}C NMR spectrum of polymer 3b in $CDCl_3$.

1.6.6 Polymer 3b

^{1}H NMR spectrum ($CDCl_3$, 500 MHz): δ 5.83 (m, 1 H); 5.27-5.33 (m, 1 H); 5.18 (m, 2H); 4.33 (m, 1 H); 4.14 (m, 1 H); 3.97 (br s, 1 H); 3.53 (m, 2H); 2.37 (m, 4H); 1.92 (m, 2H). ^{13}C NMR spectrum ($CDCl_3$, 125 MHz): δ 172.54; 172.23; 134.26; 117.54; 72.35; 70.35; 68.23; 62.89; 33.25; 32.98; 20.04.

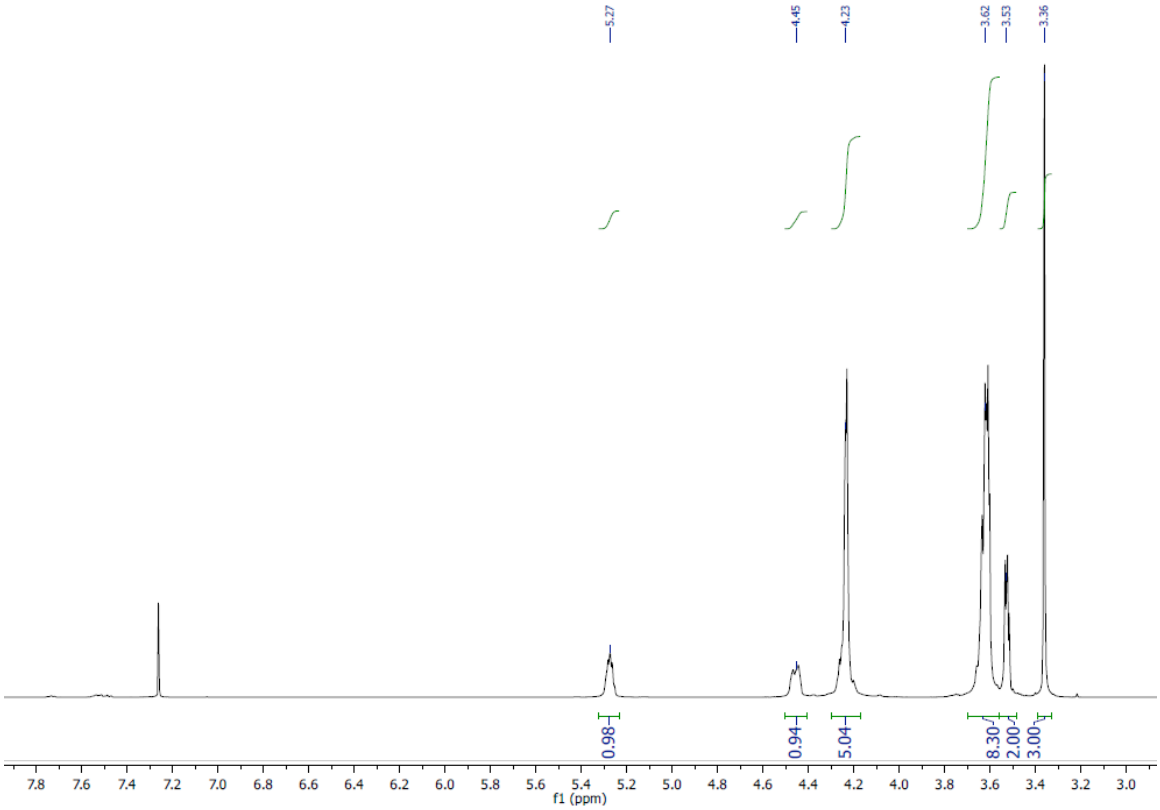

Figure S17: ^{1}H NMR spectrum of polymer 3b in $CDCl_3$.

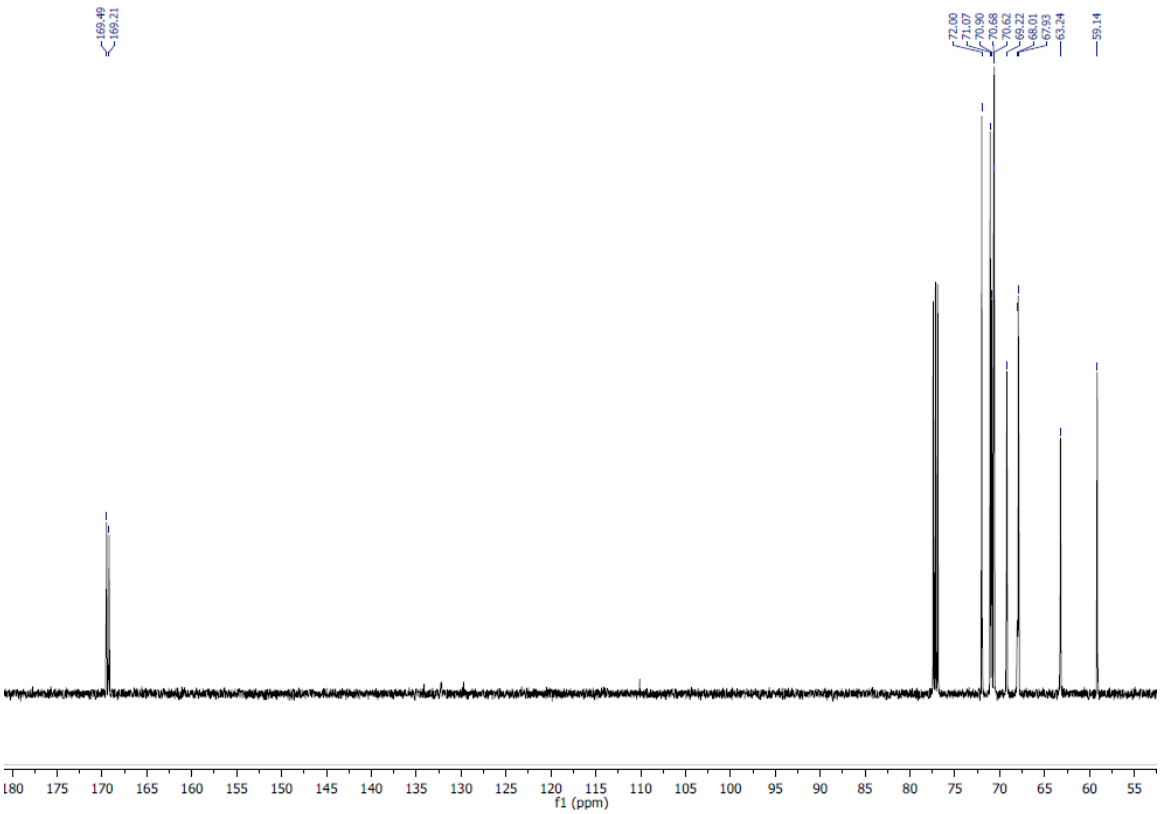

Figure S18: ^{13}C NMR spectrum of polymer 3b in $CDCl_3$.

2 Simulation Protocol Details

For PEO and each polymer in Figure 2 of the main text, two sets of simulations are performed. The first set is used to estimate the glass-transition temperature T_g for the neat polymer. The second set is used to obtain lithium-ion conductivity characteristics in the dilute-ion regime at 363 K.

To generate starting configurations for both sets of simulations, the following protocol is used. First, sixteen independent copies of a simulation cell are created. Each simulation cell contains 11-12 polymer chains, each with a molecular weight M_n of approximately 2500 g/mol (Table 1 of main text). Polymer chain configurations are generated via a self-avoiding random walk of the backbone atoms according to the rotational isomeric state approximation;[6] polymer chains are oriented randomly in the periodic, cubic simulation cell; the side length of the simulation cell is set such that the initial polymer density is 1.0 g/cm^3. To prepare systems for the study of lithium-ion conductivity, a single lithium cation is randomly inserted in four of the sixteen copies of the simulation cell The remaining twelve copies are left without a lithium cation to enable study of the neat polymer. To remove any steric clashes in the simulation cell, a steepest-descent energy minimization is run for 1,000 steps; the maximum displacement of an atom is limited to 0.1 Å per step. The resulting polymer structures are then equilibrated for 10 ns at 500 K and 1 atm and subsequently equilibrated for 25 ns at 450 K and 1 atm.

In the first set of simulations, the twelve lithium-free copies of the simulation cell are used to perform simulated dilatometry experiments[7–9] to estimate T_g. Specifically, the polymer density is monitored during cooling from 450 K to 160 K in 10 K increments. To obtain the average density at each temperature, 1 ns of dynamics is run at 1 atm and the corresponding temperature, and the last 300 ps of each temperature increment is used to obtain the average density. The intersection point between linear fits of the high-temperature and the low-temperature branches of the density-temperature curve is used to determine the T_g for the polymer. We note that the values of T_g obtained from this method are systematically high

due to the artificially fast non-equilibrium cooling used in the simulations;[7] these results thus provide a basis for comparison between polymers, rather than an absolute calculation of T_g.

In the second set of simulations, the four lithium-containing copies of the simulation cell are equilibrated at 363 K and 1 atm for 50 ns; an average density of the system is computed using the last 10 ns of each simulation. Using this fixed density for each polymer, NVT production runs of 500 ns are performed.

3 Electrochemical Characterization Details

Each polymer electrolyte is prepared by mixing neat polymer sample with lithium bis(trifluoromethane)sulfonimide (LiTFSI) salt in an argon glovebox (MBraun) in which H_2O and O_2 levels are maintained below 0.1 ppm and 1 ppm, respectively. Dry polymer and LiTFSI salt (Novolyte) are dissolved into anhydrous N-methyl-2-pyrrolidone (NMP) upon mixing at 90 ℃. The caps are removed from the vials to allow the NMP to evaporate, leaving behind a homogeneous polymer electrolyte. The polymer electrolytes are dried under vacuum for 8 hours at 90 ℃to remove any excess NMP. Most of the dry polymer electrolytes were viscous liquids at room temperature; however, polymer 1b was solid-like at room temperature. Stainless steel symmetric cells are prepared for ionic conductivity measurements of electrolytes using ac impedance spectroscopy. The dry electrolytes are contained in a cell comprised of a 254 μm-thick silicone spacer and two 200 μm-thick stainless steel electrodes. Aluminum tabs are secured to the electrodes. The entire assembly is hermetically sealed within Showa-Denko pouch material, leaving only the tab ends exposed to maintain an air- and water-free environment for the polymer electrolyte when the cell is removed from the glovebox.

Complex impedance measurements are acquired using a Biologic VMP3 potentiostat for a frequency range of 1 Hz to 1 MHz at an amplitude of 50 mV. A Nyquist plot of the impedance data is fit to an equivalent electrical circuit model to determine the electrolyte resistance. After completing the resistivity measurements, each cell is disassembled in a glovebox, and the cell thickness is measured using a micrometer. The conductivity is then calculated using the measured resistance and the geometry of the cell. Finally, the polymer electrolytes are inspected visually to confirm that no electrolyte had leaked from the cell during measurement.

4 Repeat Units and Terminal Groups for Polyesters in MD Simulations

Figure S19 illustrates the polymer repeat unit (reproduced from Figure 2 of the main text) and terminal groups that are used for the MD simulations of the polyesters. Note that if there were no terminal groups, then the terminal ether oxygen atoms would occupy the same position in the polymer repeat unit as one of the ester oxygen atoms. The tacticity of the methyl side chain in the type-1 polymers is isotatctic due to the fixed S stereochemistry of the chiral center to which it is attached. For the type-2 and -3 polymers, the stereochemistry at the chiral center is chosen randomly as S or R with equal probability such that the tacticity of the resulting chain is atactic.

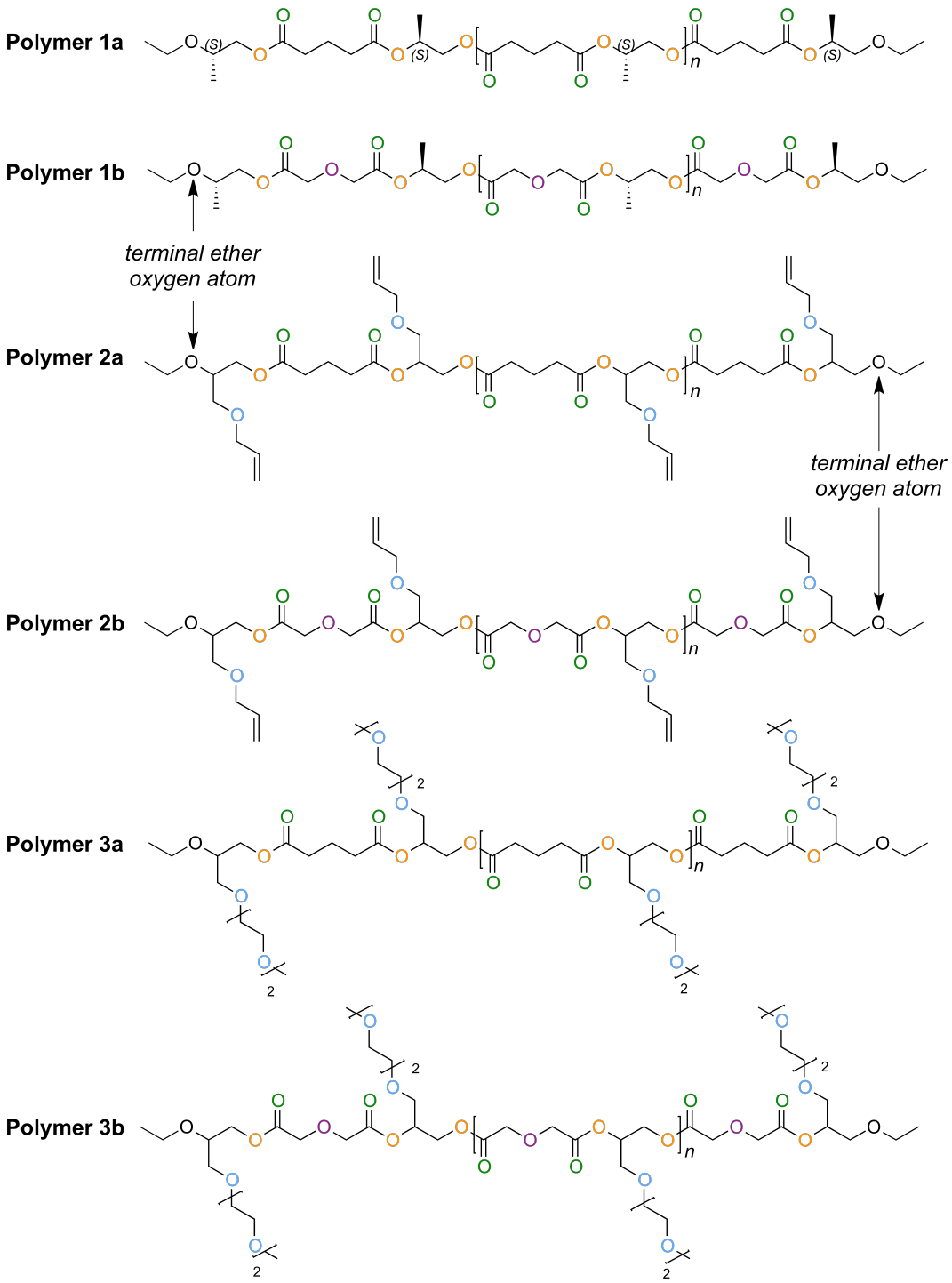

Figure S19: Repeat unit and terminal groups used in MD simulations of the polyesters.

5 Force Field Parameters for Molecular Dynamics Simulations

In this section, the parameters used to perform the MD simulations are provided. As discussed in the main text, the generalized CHARMM bonding parameters are used,[10] and the TraPPE-UA force field is used for all other inter- and intramolecular interactions between polymer atoms.[11–14] Parameters for the lithium cation are obtained from a previous simulation study.[15] Figure S20 provides reference labels for the different atom types for assigning the appropriate force field parameters.

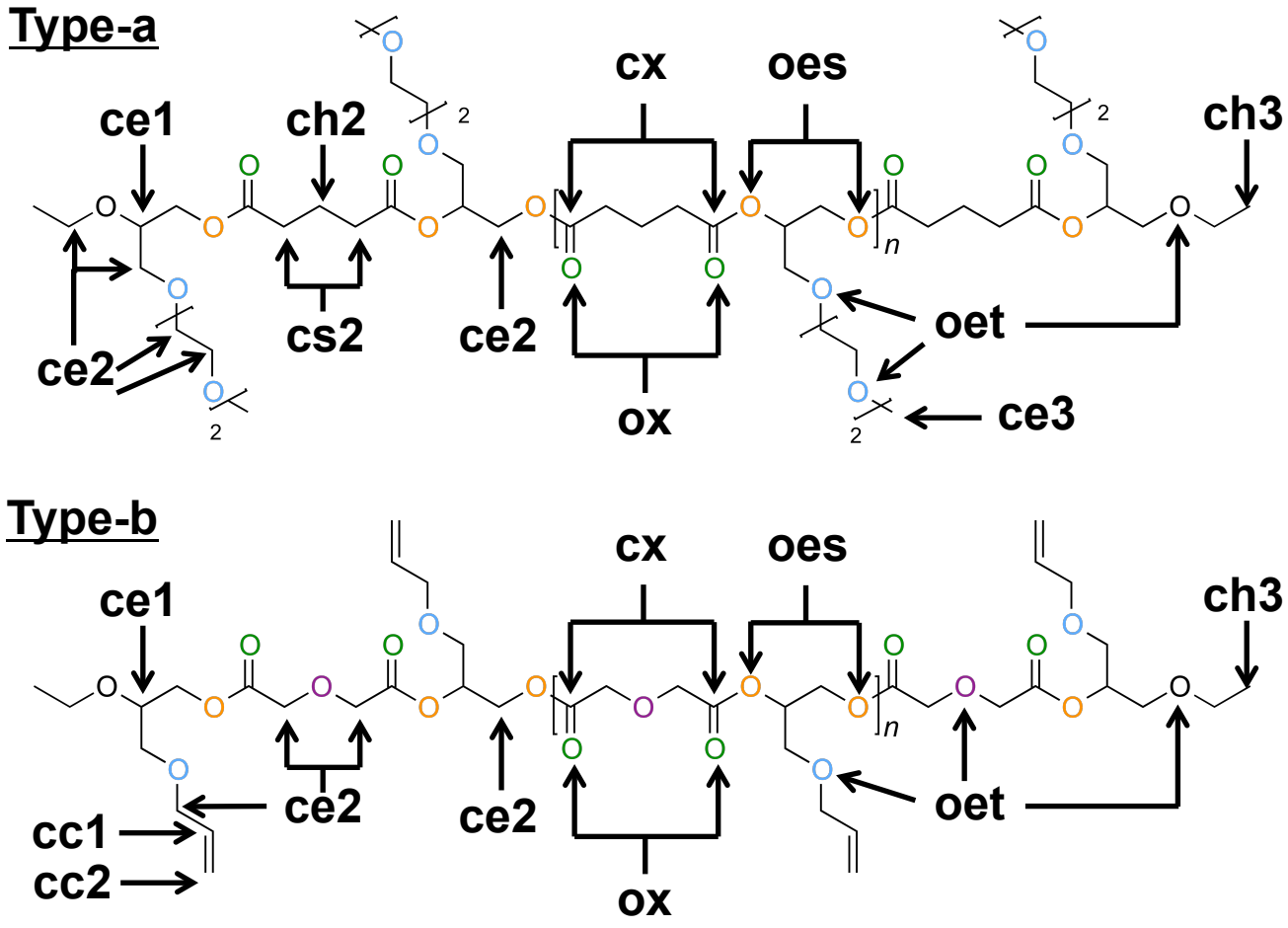

Figure S20: Reference labels for atom types in force field parameters.

5.1 Non-bonded Interaction Parameters

Non-bonded interactions are computed for all intermolecular interactions and for intramolecular interactions between atoms separated by four or more bonds and consist of pairwise additive Lennard-Jones and Coulombic potentials

$$u_{\mathrm{nb}}(r_i j) = 4\epsilon_{ij}\left[\left(\frac{\sigma_{ij}}{r_{ij}}\right)^{12} - \left(\frac{\sigma_{ij}}{r_{ij}}\right)^{6}\right] + \frac{q_i q_j}{4\pi\varepsilon_0 r_{ij}}, \tag{1}$$

where i and j denote non-bonded atoms, q_i and q_j are their respective partial charges, r_{ij} is the separation distance, σ_{ij} is the Lennard-Jones diameter, and ϵ_{ij} is the Lennard-Jones well depth. Unlike interactions are computed with Lorentz-Berthelot mixing rules:

$$\sigma_{ij} = 0.5(\sigma_{ii} + \sigma_{jj}) \quad \text{and} \quad \epsilon_{ij} = \sqrt{\epsilon_i \epsilon_j}. \tag{2}$$

Coulombic interactions between atoms separated by three bonds (1-4 interactions) are additionally computed, but the strength of the interaction is reduced by a factor of 0.5, unless otherwise noted. The parameters used in the MD simulations for these interactions are provided in Table S1.

Table S1: Non-bonded potential parameters.

atom	m (amu)	σ_{ii} (Å)	ϵ_{ii} ($\frac{\text{kcal}}{\text{mol}}$)	q (e)
ch1	13.01897	4.680	0.019872	0.00
ch2	14.02694	3.950	0.091411	0.00
ch3	15.03491	3.750	0.194746	0.00
ce1	13.01897	4.330	0.019872	0.20
ce2	14.02694	3.950	0.091411	0.20
ce3	15.03491	3.750	0.194746	0.20
cs2	14.02694	3.950	0.091411	0.00
cx0	12.01100	3.900	0.081425	0.40
cc1	13.01897	3.730	0.093399	0.00
cc2	14.02694	3.675	0.168912	0.00
oet	15.99940	2.800	0.109296	−0.50
oes	15.99940	2.800	0.109296	−0.20
ox	15.99940	3.050	0.156989	−0.40
Li^+	6.94100	1.400	0.400000	1.00

5.2 Bonding Potential Parameters

United atoms separated by a single bond interact via a harmonic bonding potential

$$u_{\text{bond}}(r_{ij}) = k_{\text{bond}}(r_{ij} - r_{ij}^{(0)})^2, \tag{3}$$

where k_{bond} is the bonding force constant, r_{ij} is the separation distance between atom i and j, and $r_{ij}^{(0)}$ is the corresponding equilibrium bonding distance. The parameters used in the MD simulations for this type of interaction are provided in Table S2.

Table S2: Bonding potential parameters for polymer atoms.

bond	k_{bond} ($\frac{\text{kcal}}{\text{mol}\cdot\text{Å}^2}$)	$r_{ij}^{(0)}$ (Å)	bond	k_{bond} ($\frac{\text{kcal}}{\text{mol}\cdot\text{Å}^2}$)	$r_{ij}^{(0)}$ (Å)
ce1 - ch3	225.0	1.540	ce1 - ce2	225.0	1.540
ce2 - ch2	225.0	1.540	ce2 - ch3	225.0	1.540
ce2 - ce2	225.0	1.540	ce2 - cc1	225.0	1.540
ce2 - cx	292.0	1.520	cs2 - cx	292.0	1.520
ch2 - ch2	225.0	1.540	ch2 - ch3	225.0	1.540
ch2 - cs2	225.0	1.540	cc1 - cc2	500.0	1.330
ce1 - oet	360.0	1.410	ce1 - oes	360.0	1.410
ce2 - oet	360.0	1.410	ce2 - oes	360.0	1.410
ce3 - oet	360.0	1.410	cs2 - oes	360.0	1.410
cx - oet	150.0	1.344	cx - oes	150.0	1.344
cx - ox	580.0	1.200			

5.3 Bending Potential Parameters

United atoms separated by a two bonds interact via a harmonic bending potential

$$u_{\text{bend}}(\theta_{ijk}) = k_{\text{bend}}(\theta_{ijk} - \theta_{ijk}^{(0)})^2, \tag{4}$$

where k_{bend} is the bending force constant, θ_{ijk} is the angle between atom i, j, and k, and $\theta_{ijk}^{(0)}$ is the corresponding equilibrium angle. The parameters used in the MD simulations for this type of interaction are provided in Table S3.

Table S3: Bending potential parameters for polymer atoms.

bend	k_{bend} ($\frac{\text{kcal}}{\text{mol}\cdot\text{rad}^2}$)	$\theta_{ijk}^{(0)}$ (degrees)	bend	k_{bend} ($\frac{\text{kcal}}{\text{mol}\cdot\text{rad}^2}$)	$\theta_{ijk}^{(0)}$ (degrees)
ch2 - ce2 - oet	49.9782	112.0	ch3 - ce1 - oes	49.9782	112.0
ch3 - ce1 - oet	49.9782	112.0	ch3 - ce2 - oet	49.9782	112.0
ch3 - ce2 - oes	49.9782	112.0	ce1 - ce2 - oes	49.9782	112.0
ce1 - ce2 - oet	49.9782	112.0	ce2 - ce1 - oes	49.9782	112.0
ce2 - ce1 - oet	49.9782	112.0	ce2 - ce2 - oet	49.9782	112.0
oet - ce2 - oet	49.9782	112.0	[a]cx - cs2 - oes	49.9782	112.0
[a]cx - ce2 - oes	49.9782	112.0	[a]cx - ce2 - oet	49.9782	112.0
[a]cc1 - ce2 - oet	49.9782	112.0	ce2 - oet - ce1	60.0136	112.0
ce2 - oes - ce2	60.0136	112.0	ce2 - oet - ce2	60.0136	112.0
ce2 - oet - ce3	60.0136	112.0	cs2 - oes - cs2	60.0136	112.0
ch2 - cs2 - cx	62.1001	115.0	ch3 - ce1 - ce2	62.1001	112.0
ch3 - ch2 - ce2	62.1001	112.0	cs2 - ch2 - cs2	62.1001	114.0
cs2 - cx - ox	62.1001	125.0	ce2 - ch2 - ce2	62.1001	114.0
ce1 - oes - cx	62.1001	115.0	ce1 - oet - cx	62.1001	115.0
ce2 - ce1 - ce2	62.1001	112.0	ce2 - cx - ox	62.1001	125.0
ce2 - oes - cx	62.1001	115.0	ce2 - oet - cx	62.1001	115.0
oes - cx - ox	62.1001	125.0	oet - cx - ox	62.1001	125.0
ce2 - cc1 - cc2	69.9695	119.7	cs2 - cx - oes	70.1483	110.0
cs2 - cx - oet	70.1483	110.0	ce2 - cx - oes	70.1483	110.0

[a]No explicit parameters are given for this bending type in the TraPPE-UA force field. These values are assumed from a similar bending potential.

5.4 Torsional Potential Parameters

United atoms separated by three bonds interact via potential given by a cosine series

$$u_{\text{tors}}(\phi_{ijkl}) = c_1\left[1+\cos\left(\phi_{ijkl}\right)\right] + c_2\left[1-\cos\left(2\phi_{ijkl}\right)\right] + c_3\left[1+\cos\left(3\phi_{ijkl}\right)\right], \tag{5}$$

where c_1, c_2, and c_3 are constant coefficients, ϕ_{ijkl} is the dihedral angle defined by atoms i, j, k, and l. The parameters used in the MD simulations for this type of interaction are provided in Table S4.

Table S4: Torsional potential parameters for polymer atoms.

torsion	c_1 ($\frac{\text{kcal}}{\text{mol}}$)	c_2 ($\frac{\text{kcal}}{\text{mol}}$)	c_3 ($\frac{\text{kcal}}{\text{mol}}$)	torsion	c_1 ($\frac{\text{kcal}}{\text{mol}}$)	c_2 ($\frac{\text{kcal}}{\text{mol}}$)	c_3 ($\frac{\text{kcal}}{\text{mol}}$)
cs2 - ch2 - cs2 - cx	1.411030	−0.271010	3.145030	ce2 - ch2 - ce2 - cx	1.411030	−0.271010	3.145030
ch2 - ce2 - oet - ce2	2.882840	−0.650809	2.218510	ch2 - ce2 - oet - ce3	2.882840	−0.650809	2.218510
ch2 - ce2 - oet - ce1	2.882840	−0.650809	2.218510	ch3 - ce1 - oes - cx	2.882840	−0.650809	2.218510
ch3 - ce1 - oet - cx	2.882840	−0.650809	2.218510	ch3 - ce2 - oet - ce1	2.882840	−0.650809	2.218510
ch3 - ce2 - oet - ce2	2.882840	−0.650809	2.218510	ch3 - ce2 - oes - ce2	2.882840	−0.650809	2.218510
ch3 - ce1 - oet - ce2	2.882840	−0.650809	2.218510	ce1 - ce2 - oes - cx	2.882840	−0.650809	2.218510
ce1 - ce2 - oet - cx	2.882840	−0.650809	2.218510	ce1 - ce2 - oet - ce2	2.882840	−0.650809	2.218510
ce1 - ce2 - oet - ce1	2.882840	−0.650809	2.218510	ce1 - ce2 - oes - ce2	2.882840	−0.650809	2.218510
ce1 - ce2 - oet - ce3	2.882840	−0.650809	2.218510	ce2 - ce1 - oes - cx	2.882840	−0.650809	2.218510
ce2 - ce1 - oet - cx	2.882840	−0.650809	2.218510	ce2 - ce2 - oet - ce3	2.882840	−0.650809	2.218510
ce2 - oes - ce2 - cx	2.882840	−0.650809	2.218510	ce2 - oet - ce2 - cx	2.882840	−0.650809	2.218510
ce2 - ce1 - oet - ce2	2.882840	−0.650809	2.218510	ce2 - ce2 - oet - ce2	2.882840	−0.650809	2.218510
ce2 - ce2 - oet - ce1	2.882840	−0.650809	2.218510	[a]ce2 - oet - ce2 - oet	2.882840	−0.650809	2.218510
[a]ce3 - oet - ce2 - oet	2.882840	−0.650809	2.218510	cs2 - oes - cs2 - cx	2.882840	−0.650809	2.218510
cc1 - ce2 - oet - ce2	2.882840	−0.650809	2.218510	[b]ce1 - oes - cx - cs2	9.689607	7.678557	1.387068
[b]ce1 - oet - cx - cs2	9.689607	7.678557	1.387068	[b]ce1 - oes - cx - ce2	9.689607	7.678557	1.387068
[b]ce1 - oet - cx - ce2	9.689607	7.678557	1.387068	[b]ce2 - oes - cx - cs2	9.689607	7.678557	1.387068
[b]ce2 - oet - cx - cs2	9.689607	7.678557	1.387068	[b]ce2 - oes - cx - ce2	9.689607	7.678557	1.387068
[b]ce2 - oet - cx - ce2	9.689607	7.678557	1.387068	[b]ce2 - oes - cx - ox	−9.669740	7.376500	−1.045270
[b]ce2 - oet - cx - ox	−9.669740	7.376500	−1.045270	[b]ce1 - oes - cx - ox	−9.669740	7.376500	−1.045270
[b]ce1 - oet - cx - ox	−9.669740	7.376500	−1.045270	[b]ch2 - cs2 - cx - ox	−0.919281	0.229800	−0.609277
[b]ch2 - ce2 - cx - ox	−0.919281	0.229800	−0.609277	[b]oes - cs2 - cx - ox	−0.919281	0.229800	−0.609277
[b]oes - ce2 - cx - ox	−0.919281	0.229800	−0.609277	[b]oet - ce2 - cx - ox	−0.919281	0.229800	−0.609277
ch2 - cs2 - cx - oes	0.919281	0.229800	0.609277	ch2 - cs2 - cx - oet	0.919281	0.229800	0.609277
oes - ce2 - cx - oes	0.919281	0.229800	0.609277	oes - ce2 - cx - oet	0.919281	0.229800	0.609277
oes - cs2 - cx - oes	0.919281	0.229800	0.609277	oes - cs2 - cx - oet	0.919281	0.229800	0.609277
oet - ce2 - cx - oes	0.919281	0.229800	0.609277	oet - ce2 - cx - oet	0.919281	0.229800	0.609277
oes - ce1 - ce2 - oes	0.000000	−1.000040	4.000127	oes - ce1 - ce2 - oet	0.000000	−1.000040	4.000127
oet - ce1 - ce2 - oes	0.000000	−1.000040	4.000127	oet - ce1 - ce2 - oet	0.000000	−1.000040	4.000127
oet - ce2 - ce2 - oet	0.000000	−1.000040	4.000127	ch3 - ce1 - ce2 - oes	0.701960	−0.211995	3.060027
ch3 - ce1 - ce2 - oet	0.701960	−0.211995	3.060027	ch3 - ch2 - ce2 - oet	0.701960	−0.211995	3.060027
ce2 - ch2 - ce2 - oet	0.701960	−0.211995	3.060027	ce2 - ce1 - ce2 - oet	0.701960	−0.211995	3.060027
ce2 - ce1 - ce2 - oes	0.701960	−0.211995	3.060027	oet - ce2 - cc1 - cc2	0.343230	−0.436271	−1.121740

[a] No explicit parameters were found for this bending type in the TraPPE-UA force field. This values are thus approximate and assumed from a similar bending potential.
[b] 1-4 intermolecular interactions involving this dihedral are set to zero.

6 Apparent Diffusivities in Simulation

Figure 3 of the main text presented the MSD results and approximate conductivities for the lithium cation in each polymer studied. Table S5 provides the apparent diffusivities evaluated at 150 ns that are used to compute the approximate conductivity values and the long-time MSD slopes on a log-log scale for each polymer. As noted in the main text, all the slopes in the long-time limit are still less than unity, although the values change somewhat depending on which time interval is used to compute the slopes.

Table S5: Simulated apparent diffusivities and MSD slopes

Polymer	$^{a}D_{\text{app}}/10^{-8}$ (cm^2/s)	^{b}log-log MSD slope
PEO	8.1 ± 3.7	0.76
1a	0.51 ± 0.07	0.59
1b	0.20 ± 0.03	0.31
2a	0.20 ± 0.03	0.90
2b	0.27 ± 0.05	0.92
3a	0.74 ± 0.12	0.31
3b	0.43 ± 0.02	0.85
1a*	0.21 ± 0.06	0.63

[a] Evaluated at $t = 150$ ns
[b] Obtained from linear fit over $t \in [100, 150$ ns$]$

Figure S21 shows the apparent diffusivity as a function of time to assess the convergence of the diffusivity values used in the conductivity calculation. The data for many of the polymers have hit a near-plateau, indicating that the values are mostly converged within error. Importantly, the relatively ordering of the apparent diffusivities for the polyesters does not change significantly with increasing time, and the apparent diffusivities for PEO is always larger than that of the polyesters by about an order of magnitude.

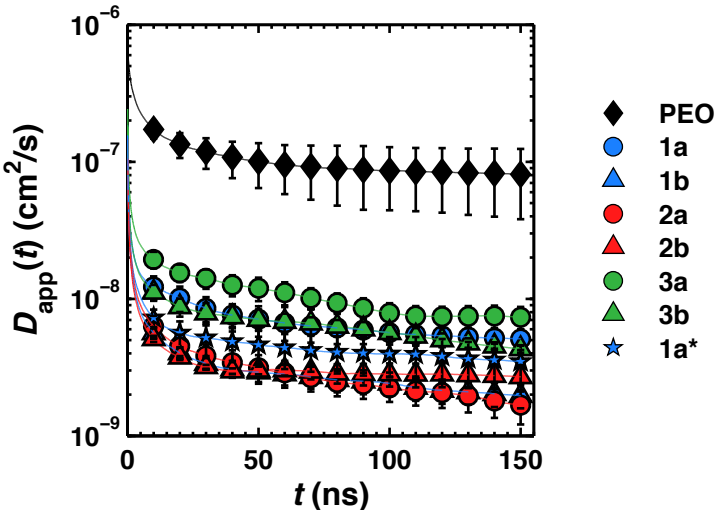

Figure S21: Apparent diffusivity for each polymer as a function of time. The error bars report standard error of the mean obtained from block-averaging from four independent trajectories, each totaling 500 ns of simulation time. The data for 1a* corresponds to simulation that adjust the strength of terminal group interactions between the polymer chain and the lithium cation (see Section X of the SI for more details on these simulations).

7 Experimental Dilute-ion Conductivities

To make a direct comparison between simulated and experimental conductivity results, dilute-ion conductivities are estimated using experimental measurements at dilute concentrations of salt. Because the oxygen density varies considerably across the polyesters, it is convenient to define a dimensionless lithium-ion concentration r as the number of lithium cations per nine polymer backbone atoms. For the polyesters, this leads to a concentration that is approximately $r = [\mathrm{Li}^+]/[\text{monomers}]$, where $[\cdots]$ denotes the number density. For PEO, this leads to a concentration that is $r = [\mathrm{Li}^+]/[\text{monomers}]/3$, since there are three PEO repeat units per nine backbone atoms. Figure S22 and Figure S23 show the measured conductivity σ as a function of r for PEO and the polyesters, respectively. The conductivity reported in both figures is obtained by subtracting the measured "background" conductivity of the pure polymers from that measured in the salt-containing polymer electrolytes. Over the concentration range shown, the data for each polymer is reasonably characterized by a least-squares linear fit, which is also shown on the figure. During the fitting, the y-intercept is constrained to be zero at $r = 0$. To obtain an estimate for the experimental conductivity, we use

$$\sigma_{\text{dilute}} = m r_{\text{sim}}, \tag{6}$$

where σ_{dilute} is the estimated dilute-ion conductivity, m is the slope of the least-squares linear fit, and r_{sim} is the lithium-ion concentration in the simulation (Table 1 of the main text). The values of m, r_{sim}, and σ_{dilute} for each polymer are provided in Table S6.

Table S6: Dilute-ion conductivity measurements.

Polymer	m (S/cm)	r_{sim}	σ_{dilute} (S/cm)
PEO	1.3×10^{-2}	0.0139	1.8×10^{-4}
1a	9.0×10^{-4}	0.0062	5.6×10^{-6}
1b	2.0×10^{-4}	0.0062	1.2×10^{-6}
2a	8.0×10^{-4}	0.0077	6.2×10^{-6}
2b	9.0×10^{-4}	0.0077	6.9×10^{-6}
3a	1.5×10^{-3}	0.0103	1.5×10^{-5}
3b	1.8×10^{-3}	0.0103	1.9×10^{-5}

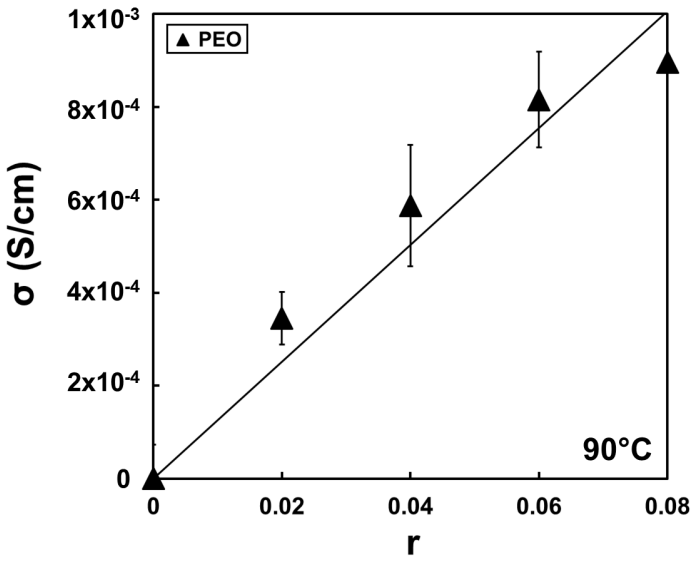

Figure S22: Linear fit of conductivity vs. r in the in dilute regime for PEO. All data shown are for 363 K.

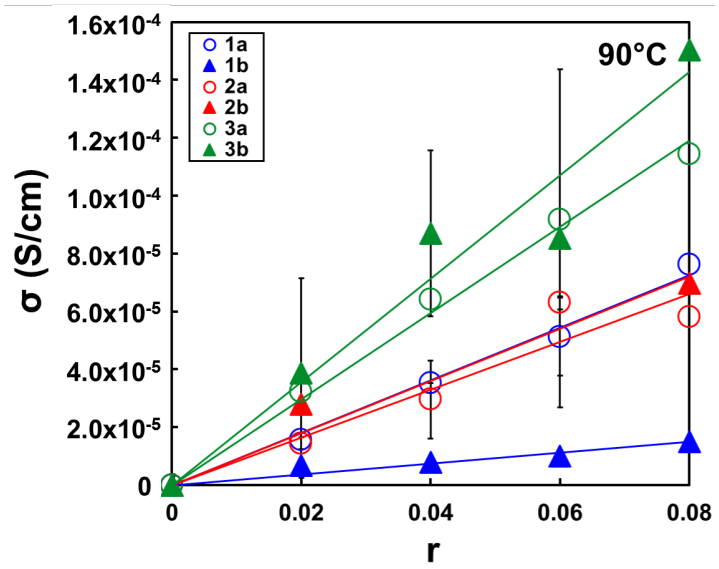

Figure S23: Linear fit of conductivity vs. r in the in dilute regime for polyesters. All data shown are for 363 K.

8 Effect of Terminal Group Interactions in Polymer 1a

As discussed regarding Figure 6b of the main text, the ether contribution for the type-a polymers must be due to the terminal groups of the polymer chain (Figure S19). This indicates that the lithium cation interact strongly with these terminal groups in some of the MD trajectories. Although this effect should diminish for chains with higher molecular weights, these results suggest that the terminal groups can affect the lithium-ion coordination environment in electrolytes with short polymer chains, which could be a consideration in experimental samples, although the terminal groups of polymer chains are often unknown during synthesis,

To assess the degree to which these interactions might bias the simulation results of lithium-ion conductivity, an additional set of simulations were performed for polymer 1a. For this additional set of simulations, the procedure for preparation, equilibration, and simulation is identical to that outlined in the Methods section of the main text except for a minor modification to the force field parameters for a subset of atoms. Namely, the ether oxygen atoms in the terminal groups are treated as if they are ester oxygens that are part of the normal polymer repeat unit.

Figure S24 provides a comparison of results obtained with and without the modified treatment of terminal oxygen atoms. Figure S24a, which includes data from Figure 3a, reveals that the rate of lithium-ion diffusion in simulations of polymer 1a with the modified treatment is slightly slower than the standard treatment of terminal groups by a factor of less than 1.5. Additionally, lithium-ion diffusion in polymer 1a with the modified treatment is marginally faster than that in polymer 1b, though the two results are within error of one another, such that the trends between type-a and -b polymers are largely unaffected. The slower diffusion rate with the modified treatment is expected because the lithium cation is no longer coordinated by the polymer chain ends, which are expected to be more mobile on subdiffusive timescales.. Figure S24b, which is a reproduction of Figure 4 of the main text with the additional data for polymer 1a included, show that the modified treatment of the

terminal atoms somewhat improves the correlation with experiment for polymer 1a. Overall, we conclude that the effect of the terminal group interactions in polymer 1a is minor.

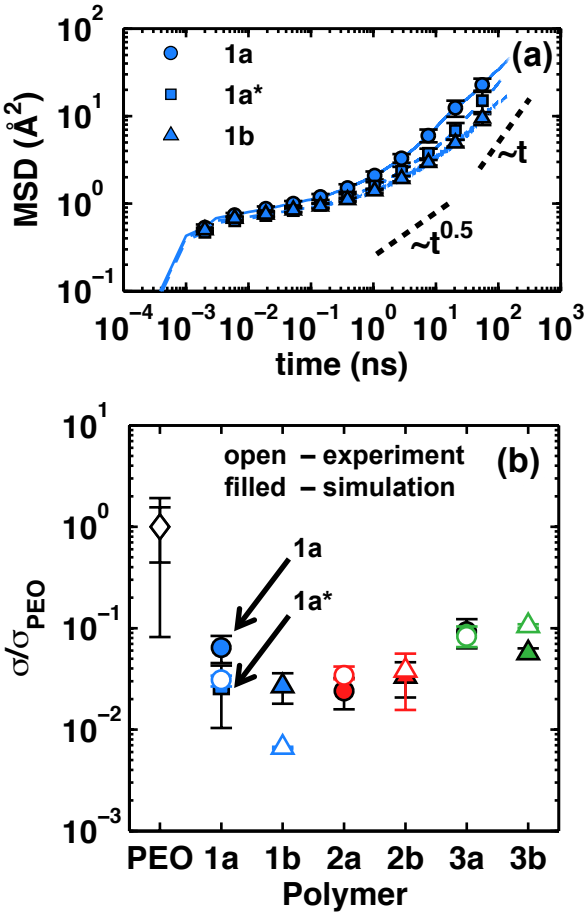

Figure S24: Analysis of terminal group effects on lithium-ion transport. (a) Lithium-ion mean square-displacement (MSD) in the dilute ion limit at 363 K for polymer 1a and polymer 1b. (b) Comparison of ionic conductivities at 363 K; all data is normalized to the corresponding conductivity of PEO. The asterisk denotes results for simulations in which the terminal oxygen atoms are treated as ester oxygens in the polymer repeat unit.

9 Correlation between T_g and Conductivity in MD Simulations

Figure S25 presents the MD simulation analogue of Figure 5b of the main text. The figure illustrates the same trend as in experiment. Namely, the conductivity of PEO, when compared to the polyesters, is far higher than can be explained on the basis of its relative glass transition temperature.

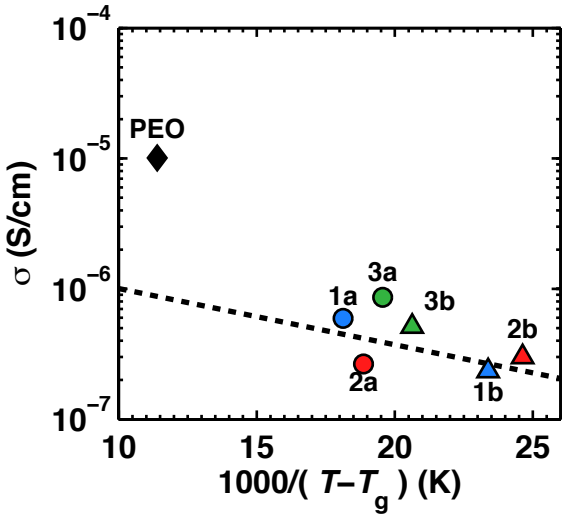

Figure S25: Correlation between dilute-ion conductivity and the inverse temperature difference from T_g at $T = 363$ K K (simulation results). The dashed line indicates the linear fit of the data for the polyesters.

10 Radial Distribution Functions for all Polymers

Figure S26 presents pair radial distribution functions (RDFs) for the lithium cation and each type of oxygen atom for all the polyesters and also PEO. The figure shows that there are clear compositional differences between the first and second solvation shells in the polyesters.

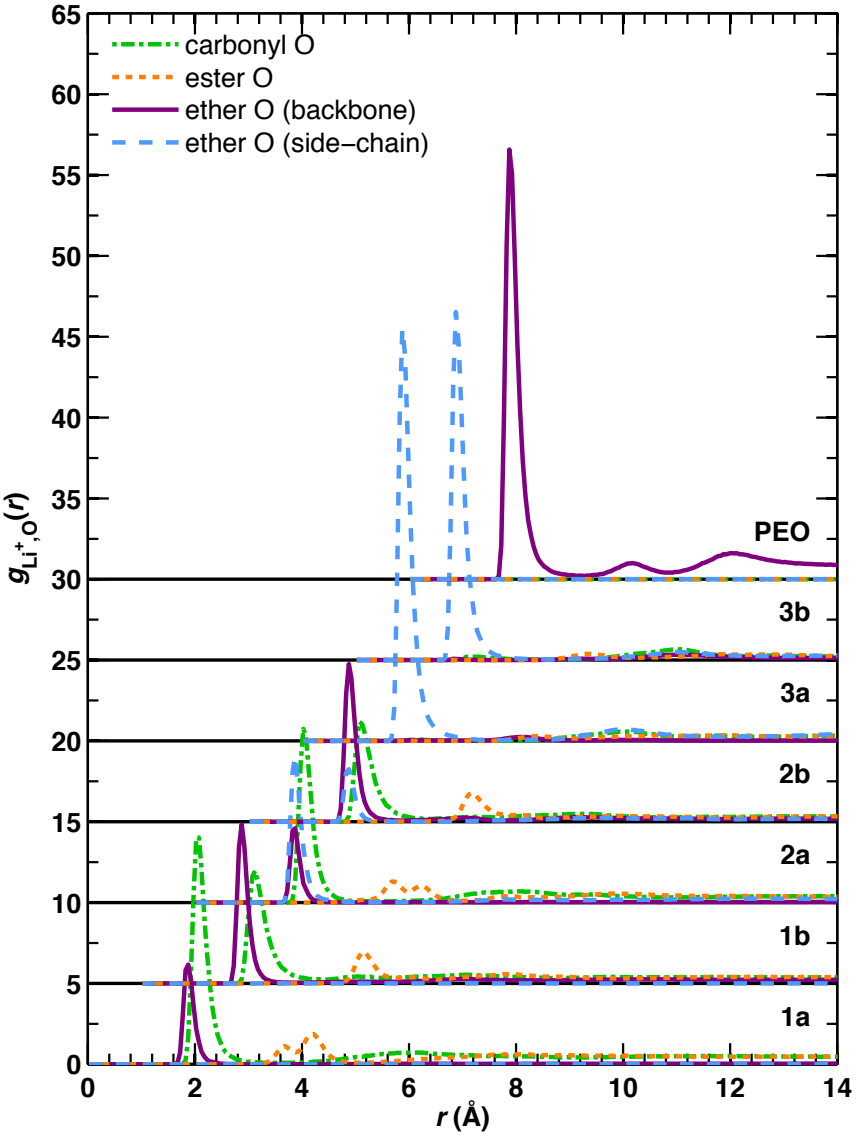

Figure S26: Lithium cation-oxygen radial distribution functions $g_{\mathrm{Li^+,O}}(r)$ for different oxygen types in each polymer. The $g_{\mathrm{Li^+,O}}(r)$ for each oxygen type is normalized with respect to the total oxygen number density in the polymer. Following the dataset for polymer 1a, each subsequent dataset is artificially shifted vertically (by 5 units) and horizontally (by 1 Å) for clarity.

11 Side chain Localization of Lithium Cation in Polymer 3a

Figure S27 shows an analogue of Figure 6 of the main text but with PEO compared to polymer 3a rather than polymer 3b. As in Figure 6 of the main text, the coordination lines for polymer 3a are static and also predominantly formed from ether oxygens on the side chains. The lithium-ion diffusion in polymer 3a is thus limited to rare inter-chain hopping events, between which the lithium cation is localized to the side chains.

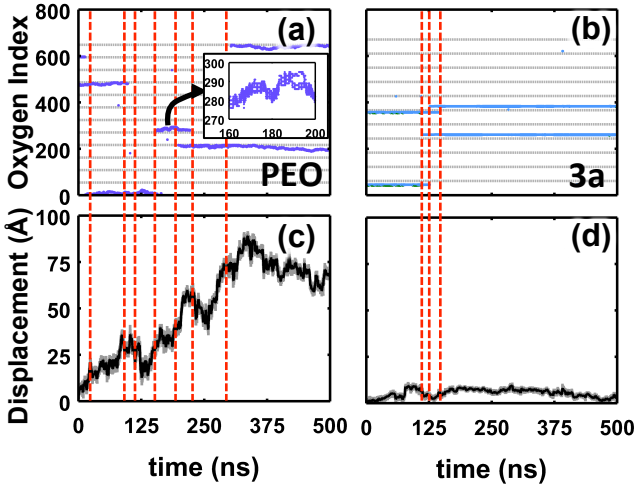

Figure S27: Analysis of changes in lithium-ion coordination with changes in lithium-ion position. Lithium-ion coordination environment for (a) PEO and (b) polymer 3a (markers denote coordination with oxygen for at least half of a 100-ps interval). The horizontal gray lines demarcate separate polymer chains. The inset in (a) illustrates the coordination over a 40 ns segment in the trajectory. Lithium-ion displacement from initial position in (c) PEO and (d) polymer 3b. The gray curve indicates the instantaneous displacement from the initial position, and black curve indicates the rolling average over 100-ps intervals. Vertical, red lines highlight inter-chain hopping events.

12 Backbone Localization of Lithium Cation in Type-1 and -2 Polymers

Figure S28 shows the lithium-ion coordination environment during individual trajectories for type-1 and type-2 polymers by tracking the indices of oxygen atoms that are within 3.25 Å of the lithium cation, similarly to Figure 7a and 7b of the main text. The data for the type-a polymers reveals that carbonyl oxygens (green) predominantly coordinate the lithium cation. For polymer 2a, ether oxygens on the side chain (light blue) also coordinate with lithium cation at times but never without the presence of carbonyl oxygens. Observations are similar for the type-b polymers except that the ether oxygen that is between the two carbonyl groups (purple) also coordinates the lithium cation. Thus, we find that the lithium-cation is mostly localized to the polymer backbones for the type-1 and -2 polymers.

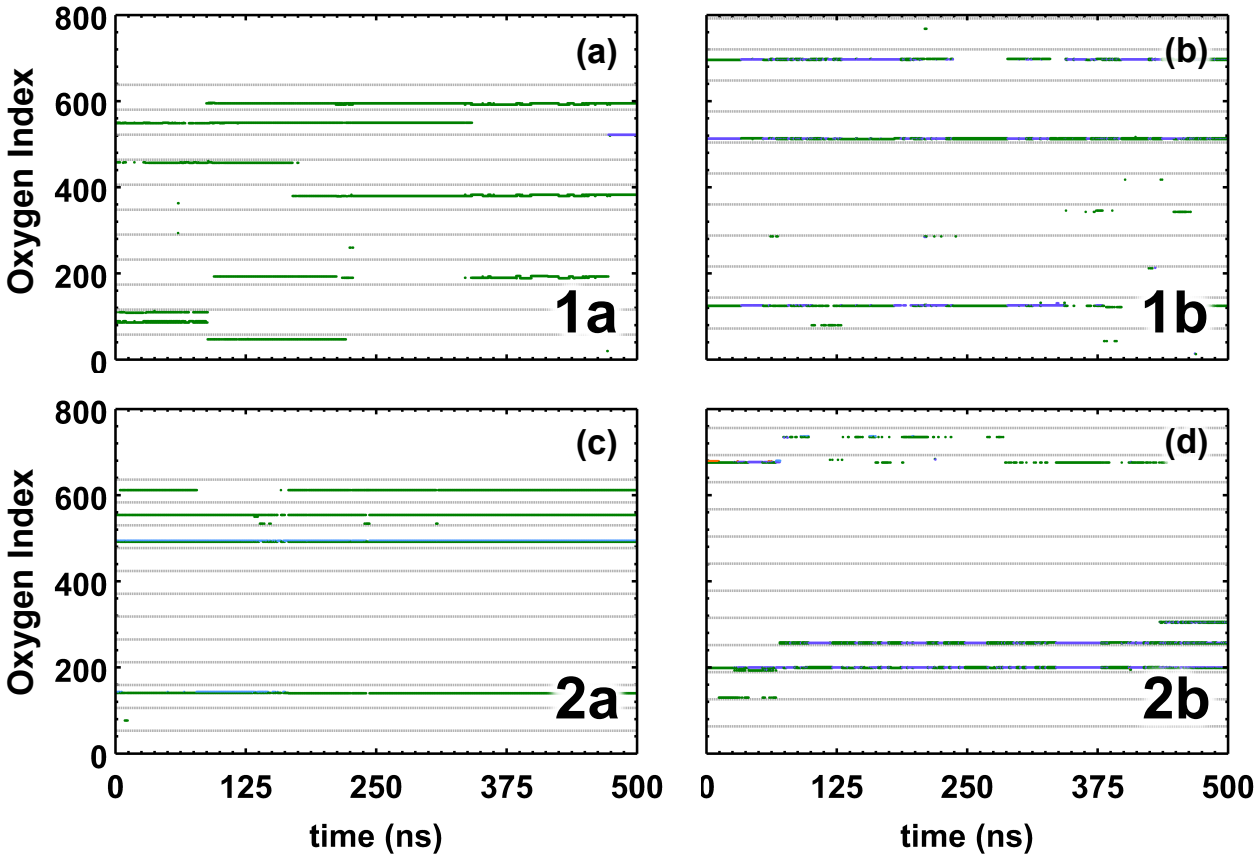

Figure S28: Lithium-ion coordination with oxygen atoms during a molecular dynamics trajectory for (a) polymer 1a, (b) polymer 1b, (c) polymer 2a, and (d) polymer 2b. The color scheme for the oxygen atoms is the same as that in Figure 2 and Figure 6b of the main text.

13 Comparison of Solvation-Site Networks

Figure S29 presents a pictorial representation of viable solvation sites in all the polymers studied. Viable solvation sites are identified from polymer configurations if a set of oxygen atoms are each within 3.7 Å of the centroid of that set. For polymer 1a, sites are identified using sets of five carbonyl oxygens. For polymer 1b, sites are identified using sets of four carbonyl and two ether oxygens or sets of three carbonyl and three ether oxygens. For polymer 2a, sites are identified using sets of four carbonyl and one ether oxygen, sets of three carbonyl and two ether oxygens, sets of two carbonyl and three ether oxygens, and sets of one carbonyl and three ether oxygens. For polymer 2b, sites are identified using sets of three carbonyl and three ether oxygens, sets of two carbonyl and three ether oxygens, or sets of four carbonyl and two ether oxygens. For polymer 3a, sites are identified using sets of five ether oxygens. For polymer 3b, sites are identified using sets of five ether oxygens. For PEO, sites are identified using of five ether oxygens. The figure makes clear, within the limitations of this identification protocol, the sparsity of the solvation-site networks for the polyesters relative to that of PEO.

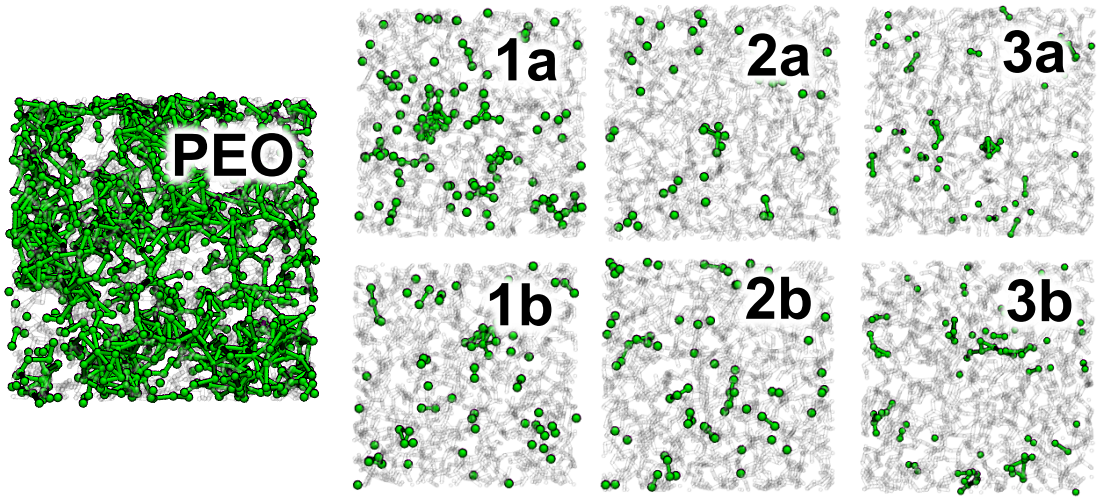

Figure S29: Depiction of sites in each polymer that are consistent with the most common binding motifs (green circles). Two sites are connected by lines if they are within 3 Å to illustrate the relative connectivity densities. The polymer configuration is the transparent representation.

References

(1) Feng, L.; Hao, J.; Xiong, C.; Deng, X. *Chem. Commun.* **2009**, 4411–4413.

(2) Cohen, C. T.; Chu, T.; Coates, G. W. *Journal of the American Chemical Society* **2005**, *127*, 10869–10878, PMID: 16076192.

(3) Larrow, J. F.; Jacobsen, E. N.; Gao, Y.; Hong, Y.; Nie, X.; Zepp, C. M. *The Journal of Organic Chemistry* **1994**, *59*, 1939–1942.

(4) Peilstöcker, K.; Marhold, A. Fluorinated benzaldehydes. 2005; `https://www.google.com/patents/US6903239`.

(5) Longo, J. M.; DiCiccio, A. M.; Coates, G. W. *Journal of the American Chemical Society* **2014**, *136*, 15897–15900, PMID: 25366127.

(6) Flory, P. *Statistical mechanics of chain molecules*; Interscience Publishers, 1969.

(7) Buchholz, J.; Paul, W.; Varnik, F.; Binder, K. *The Journal of Chemical Physics* **2002**, *117*, 7364–7372.

(8) Han, J.; Gee, R. H.; Boyd, R. H. *Macromolecules* **1994**, *27*, 7781–7784.

(9) Wu, C. *The Journal of Physical Chemistry B* **2011**, *115*, 11044–11052, PMID: 21859139.

(10) Vanommeslaeghe, K.; Hatcher, E.; Acharya, C.; Kundu, S.; Zhong, S.; Shim, J.; Darian, E.; Guvench, O.; Lopes, P.; Vorobyov, I.; Mackerell, A. D. *Journal of Computational Chemistry* **2010**, *31*, 671–690.

(11) Martin, M. G.; Siepmann, J. I. *The Journal of Physical Chemistry B* **1999**, *103*, 4508–4517.

(12) Wick, C. D.; Martin, M. G.; Siepmann, J. I. *The Journal of Physical Chemistry B* **2000**, *104*, 8008–8016.

(13) Stubbs, J. M.; Potoff, J. J.; Siepmann, J. I. *The Journal of Physical Chemistry B* **2004**, *108*, 17596–17605.

(14) Kamath, G.; Robinson, J.; Potoff, J. J. *Fluid Phase Equilibria* **2006**, *240*, 46 – 55.

(15) Wu, H.; Wick, C. D. *Macromolecules* **2010**, *43*, 3502–3510.